12

The Interaction Region

Contents

12.1 Introduction 816
12.2 The Luminosity Spectrum 817
12.2.1 Beam Energy Spread 817
12.2.2 Initial State Radiation 817
12.2.3 Beamstrahlung 818
12.2.4 Measurement of the Luminosity Spectrum 822
12.3 Detector Background Sources 823
12.3.1 Beamstrahlung-produced e^+e^- Pairs 823
12.3.2 Hadronic Backgrounds from $\gamma\gamma$ Interactions 827
12.3.3 Quadrupole and Bend Synchrotron Radiation 827
12.3.4 Muon Backgrounds 832
12.4 Detector Issues 836
12.4.1 Effect of Backgrounds on the Detector 837
12.4.2 Vibration Suppression for the Final Focus Quadrupoles 844
12.4.3 Measurement of Sub-nm Displacements by means of a Laser Interferometer 847
12.4.4 An Optical Anchor for the Final Quadrupoles 849
12.4.5 SLD Final Focus Quadrupole Vibration Measurements 850
12.4.6 Measurement of Polarization and Beam Energy 850
12.5 Conclusions 851

12.1 Introduction

Table 12-1 summarizes some of the machine design parameters important to the physics capabilities of the NLC and to the design of the interaction region (IR) and detector. Three sets of parameters are considered for each of the two machine energies. They define a volume in parameter space within which the luminosity is roughly constant.

Depending on the exact performance of each of the NLC's subcomponents, we will find ourselves somewhere in that space. The rf power system controls the bunch charge and the number of bunches that can be accelerated each machine cycle. The bunch compression system and requirements on momentum spread will determine the minimum bunch length, σ_z. The final doublet β functions, β_x and β_y, must be larger than σ_z. The invariant emittance in y depends on the performance of the damping rings and on how well the linac and final focus can transport a low-emittance beam. The final value of ϵ_y achieved, together with β_y, will determine the value of the y spot size, σ_y. This in turn will set the scale for vibration tolerance and field stability of the final quadrupoles. Assuming the damping rings provide the specified ϵ_x, β_x is a semifree parameter, adjusted to give the desired luminosity while keeping deleterious beam-beam interaction effects to an acceptable level.

The choice of X-band rf for the NLC sets the interbunch separation at 1.4 ns (or 42 cm). To have each bunch interact only with its partner, there must be a crossing angle at the IP. This crossing angle is put into the NLC at the big bend, just after the collimation section located after the linac and before the final focus. The bend angle then also helps to reduce the muon flux that results when the beam interacts with the collimators. The size of the collimator apertures are measured in terms of the number of beam widths. Physical limitations and wakefield effects imply minimum collimator apertures corresponding to $7\sigma_x \times 35\sigma_y$. Beam tails and these apertures determine the level of muons produced. The apertures, the final-focus lattice, and assumptions on what the non-Gaussian profile of the beam may be determine the production of synchrotron radiation (SR). The design of the masking system and the value of detector's solenoidal field control the backgrounds caused by the SR photons.

The high charge density in each bunch causes particles in one bunch to interact with the overall field of the opposing bunch. This beam-beam interaction results in a luminosity enhancement as the beams are attracted to each other. The resulting acceleration, however, results in the copious production of photons, which will smear the luminosity spectrum as a function of $\sqrt{s}$. The photons can themselves interact coherently with the field of the opposing bunch, or interact with the individual $e^{\pm}$ of the opposing bunch to produce e^+e^- pairs. While predominately produced at low p_t, these pairs can cause problems in the detector and must also be controlled by the solenoidal field and the masking. The $\gamma\gamma$ interactions can cause the production of jets of hadrons with high p_t. The problem is exacerbated by the 1.4-ns bunch structure of the NLC. Particle detectors with good timing resolution will be required to separate the background hits arising from other bunches in the train from those hits produced in the interaction that caused the trigger. Trigger schemes may need to be developed to control the rate at which these backgrounds trigger the detector.

The issue of dealing with the 3.6–7.0-nm y-spot sizes strongly affects the discussion of the IR. The source terms in the problem are the naturally occurring ground vibrations and ground motion driven by local laboratory sources, such as pumps and the flow of cooling fluids. The support structures which stabilize the final doublet against vibration at the nm level will reside within the detector. Any device that might be required to sense or control the inertial or relative movement of the the quadrupoles must be accommodated by the detector. Finally, detectors usually use various fluids to cool their magnet coil and electronics; the influence of fluid flow on the final-doublet vibration will need to be understood.

	500 GeV			1 TeV		
	A	B	C	A	B	C
Trains/s		180			120	
Bunches/train		90			90	
Interbunch spacing (ns)		1.4			1.4	
Electrons/bunch (10^{10})	0.65	0.75	0.85	0.95	1.1	1.25
σ_x-spot size (nm)	256	286	286	202	221	256
σ_y-spot size (nm)	4.23	5.25	6.71	3.39	4.11	5.15
σ_z-spot size (μm)	100	125	150	125	150	150
x beam divergence (μrad)	32.0	28.6	28.6	20.2	18.5	16.0
y beam divergence (μrad)	33.8	35.0	33.5	27.1	27.4	25.8
Minimum collimator apertures	$7\sigma_x \times 35\sigma_y$			$7\sigma_x \times 35\sigma_y$		
$\mathcal{L}$ (geometric) ($10^{33}\,\mathrm{cm}^{-2}\ \mathrm{s}^{-1}$)	5.0	4.8	4.9	11.3	11.4	10.2
H_D - Luminosity Enhancement Factor	1.46	1.45	1.52	1.41	1.43	1.53
$\mathcal{L}$ (with pinch) ($10^{33}\,\mathrm{cm}^{-2}\ \mathrm{s}^{-1}$)	7.3	7.0	7.4	16.0	16.4	15.6

Table 12-1. *List of the NLC parameters that define the operating range of the interaction region and detector.*

12.2 The Luminosity Spectrum

Ideally, the beam energy at the NLC would be a delta function at the design energy. It could then trivially be used as a constraint in any physics analysis. The finite energy spread of the NLC, initial-state radiation effects, and the production of photons in the beam-beam interaction will degrade the delta function to a spectrum. The spectrum can be unfolded from any physics analysis if it is not too broad, where "too" is determined by the specific physics channel of interest, and if we can accurately measure the spectrum.

12.2.1 Beam Energy Spread

Figure 12-1 shows the expected beam energy spread at the IP for the 1-TeV machines. The shape comes from the bunch compression that sets the beam spot size in z. It is similar for the 500-GeV machine.

12.2.2 Initial State Radiation

At the NLC, the effects of initial-state radiation (ISR) will be about the same as that at SLC or LEP II. The scale of the problem is set by the variable $L = \ln \frac{s}{m_e^2}$. L varies from 24.2 to 27.6, 29.0, or 29.8 as $\sqrt{s}$ goes from m_z to 500, 1000, or 1500 GeV. The amount of ISR is irreducible and therefore sets the scale for how small the luminosity smearing due to the beam energy spread and the beamstrahlung must be. The electron energy distribution, $D_e(z,s)$, in the presence of ISR has been calculated by Fadin and Kuraev [Kuraev, 1985]. (See their Eqs. (20) and (21)). Here $\sqrt{s}$ is the center-of-mass energy of the interacting e^+ and e^- and z is the fractional e^+ or e^- energy following ISR.

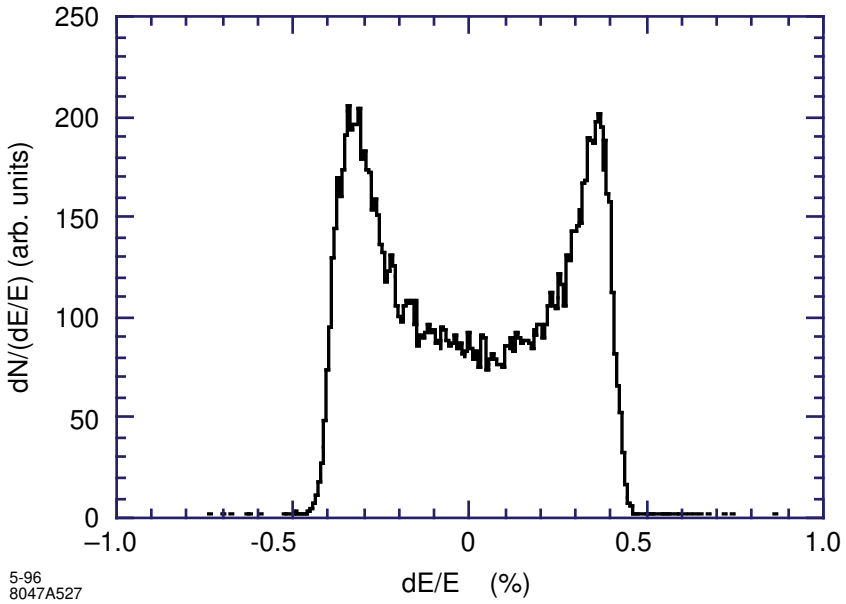

Figure 12-1. *Beam energy spread for the 1-TeV lattice.*

The cross section has the form,

$$\sigma(s) \propto \int\int dx_1 dx_2 D(x_1,s) D(x_2,s) \sigma(s x_1 x_2). \tag{12.1}$$

Defining $sx_1x_2 = (1-x)s$ and integrating at fixed x yields,

$$\sigma(s) = \int dx \sigma(s(1-x)) F(x,s), \tag{12.2}$$

where $F(x,s)$ (Eq. (28) of Fadin & Kuraev) represents the luminosity distribution function.

The dashed curve in Figure 12-2 shows the electron momentum distribution function, $D_e(z,s)$, plotted for $\sqrt{s}$=500 GeV as a function of $z = p_{\rm beam}/p_{\rm max}$, the fractional lepton momentum. The solid curve shows the luminosity spectrum $F(x,s)$ for $\sqrt{s}_{\rm max} = 500$ GeV, plotted as a function of $z = \sqrt{s}/\sqrt{s}_{\rm max}$. Here $1-z = \sqrt{1-x}$. Each curve is normalized to unit area. When plotted as in Figure 12-2, one cannot distinguish any difference in either the electron momentum distribution function or in the luminosity distribution over the range of $\sqrt{s}$ considered. Any small differences can be seen by examining Table 12-2, which shows the fraction of the luminosity within 0.1%, 0.5%, 1%, 5%, and 10% of the nominal center-of-mass energy, as well as the mean energy loss and the rms energy spread, for each of the four values of $\sqrt{s}$ considered.

12.2.3 Beamstrahlung

As one bunch of beam particles passes through the electromagnetic field of the opposing bunch, radiation will be emitted. The photons thus produced are called "beamstrahlung" photons. The subject has been extensively discussed in the literature. The results herein are taken from Ref. [Chen, 1990] and Ref. [Chen, 1992].

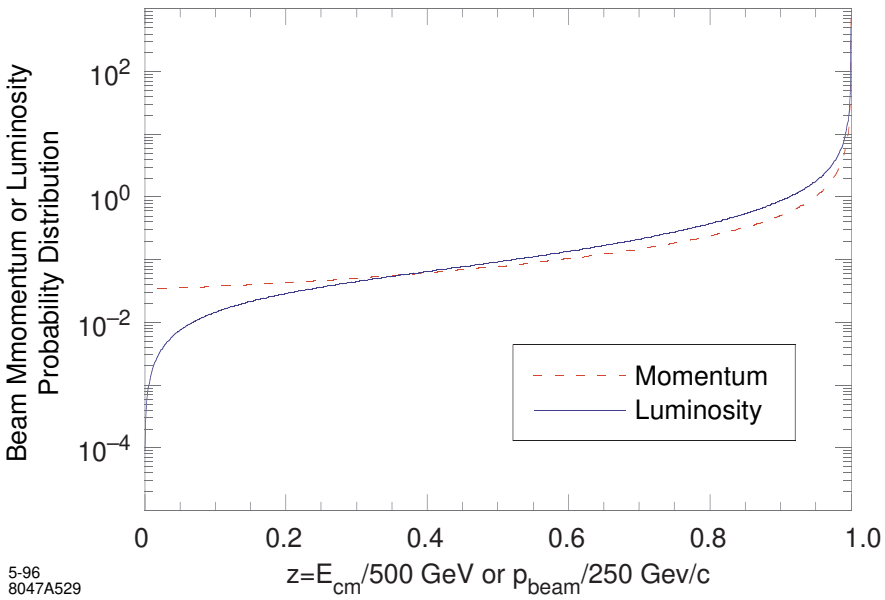

Figure 12-2. *The dashed curve shows the electron momentum distribution as a function of the normalized electron momentum after ISR. The solid curve shows the luminosity distribution after ISR as a function of the normalized center of mass energy. While the plot corresponds to a center of mass energy of 500 GeV, no difference would be visible for any center of mass energy between m_Z and 1.5 TeV.*

	m_Z	500 GeV	1 TeV	1.5 TeV
Mean e^+e^- c.m. energy loss	4.19%	4.77%	5.00%	5.14%
Rms e^+e^- c.m. energy spread	11.2%	11.9%	12.2%	12.4%
% of $\mathcal{L}$ within 0.1% of $\sqrt{s}_{\rm nom}$	54.7%	50.1%	48.3%	47.3%
% of $\mathcal{L}$ within 0.5% of $\sqrt{s}_{\rm nom}$	65.2%	61.2%	59.6%	58.7%
% of $\mathcal{L}$ within 1% of $\sqrt{s}_{\rm nom}$	70.2%	66.6%	65.2%	64.4%
% of $\mathcal{L}$ within 5% of $\sqrt{s}_{\rm nom}$	82.8%	80.5%	79.6%	79.1%
% of $\mathcal{L}$ within 10% of $\sqrt{s}_{\rm nom}$	88.3%	86.7%	86.0%	85.6%

Table 12-2. *Effect of ISR on e^+e^- luminosity spectra.*

The production of beamstrahlung photons is a stochastic process. The probability that a given particle will radiate and the characteristic energy of the radiation are determined by the field density or equivalently by the number of electrons or positrons per bunch and the bunch dimensions. When this density is high relative to the critical electric field, beamstrahlung is more likely to occur. The critical electric field, $E_{\rm critical}$, is defined as that field which, when an electron travels one Compton wavelength in it, does an amount of work equal to $m_e c^2$:

$$eE_{\rm critical}\lambda_c \equiv m_e c^2 \tag{12.3}$$

The magnetic field equivalent is:

$$B_{\rm critical} = \frac{\alpha e}{r_e^2} \sim 4.4 \times 10^9 \text{ Tesla} \tag{12.4}$$

The field strength is measured in terms of the dimensionless quantity

$$\Upsilon \equiv \frac{\gamma B_{\rm bunch}}{B_{\rm critical}} = \frac{E_{\rm bunch}}{E_{\rm critical}} \tag{12.5}$$

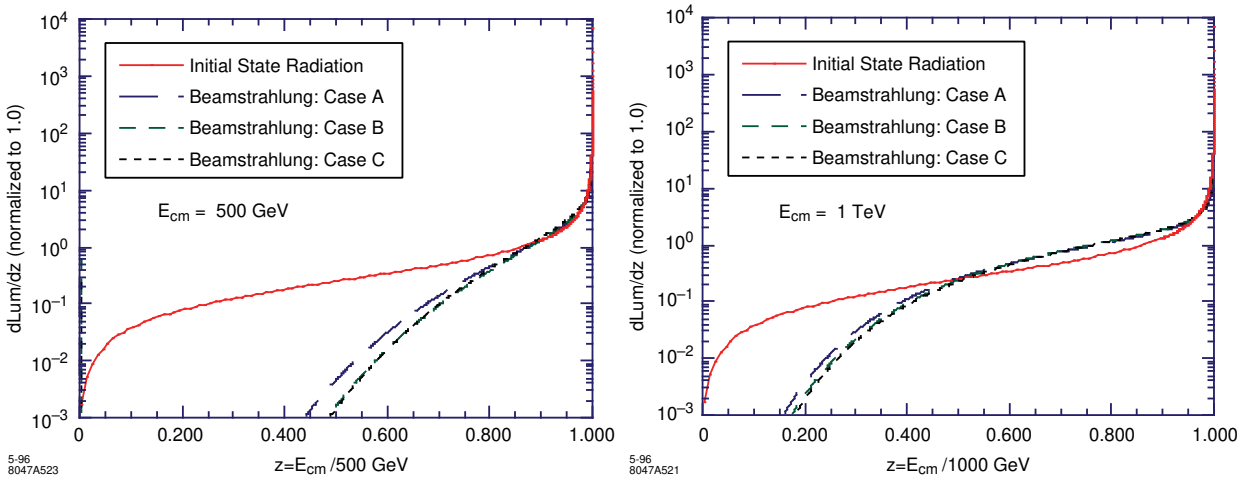

Figure 12-3. *The luminosity spectrum after beamstrahlung at 500 GeV and 1 TeV for the three parameter sets under consideration. The spectrum due to initial state radiation is presented for comparison.*

where

$$B_{bunch} \cong \frac{5eN_e}{6\sigma_z\,(\sigma_x+\sigma_y)} \quad . \tag{12.6}$$

In Ref. [Chen, 1992], Chen derives an expression (see his Eq.(24)) for the differential luminosity which is composed of three parts, corresponding to the cases when either no, one, or more than one photon is emitted. Each part is expressed in terms of N_γ, the mean number of photons produced per electron,

$$N_\gamma = \frac{5}{2}\frac{\alpha\sigma_Z}{\gamma\lambda_c}\Upsilon\left(1+\Upsilon^{2/3}\right)^{-1/2} . \tag{12.7}$$

The shape of the curve is generally described by N_γ, by the average energy loss per electron, δ_b

$$\delta_\mathrm{b} = \frac{1}{2}N_\gamma\Upsilon\frac{(1+\Upsilon^{2/3})^{1/2}}{(1+(\frac{3}{2}\Upsilon)^{2/3})^2} \quad , \tag{12.8}$$

and by the fraction of the luminosity at the full nominal beam energy,

$$\frac{1}{N_\gamma^2}\left[1-e^{N_\gamma}\right]^2 \quad . \tag{12.9}$$

In Figure 12-3, we plot the luminosity spectra for the three parameter sets at 500 GeV and 1 TeV. The ISR curve is added for comparison. In Figure 12-4, the region of the luminosity spectra within 2% of the nominal beam energy is plotted for the three parameter sets at 500 GeV and 1 TeV. Figure 12-5 presents a comparison of Case A for the 500-GeV and 1-TeV machines.

Table 12-3 summarizes the situation by listing the values of Υ, N_γ, δ_b, and the fraction of the luminosity within 0%, 0.1%, 0.5%, 1%, 5%, and 10% of the nominal center of mass energy. The fraction at 0% is taken from the above expression, while the others are obtained by integrating the distributions in Figure 12-3,

The machine parameter sets have been chosen so that the beamstrahlung induced smearing of the luminosity spectrum is not substantially worse than the luminosity smearing due to ISR. As the ISR part of the smearing

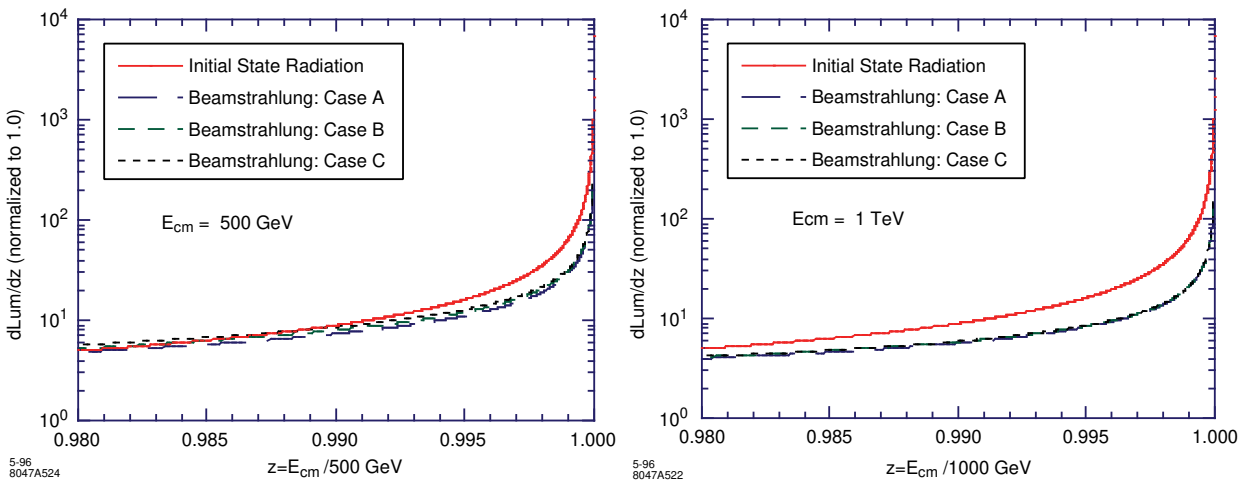

Figure 12-4. *A closeup of the region of the luminosity spectrum due to beamstrahlung near the nominal beam energy at 500 GeV and 1 TeV for the parameter sets listed previously. The spectrum due to ISR is presented for comparison.*

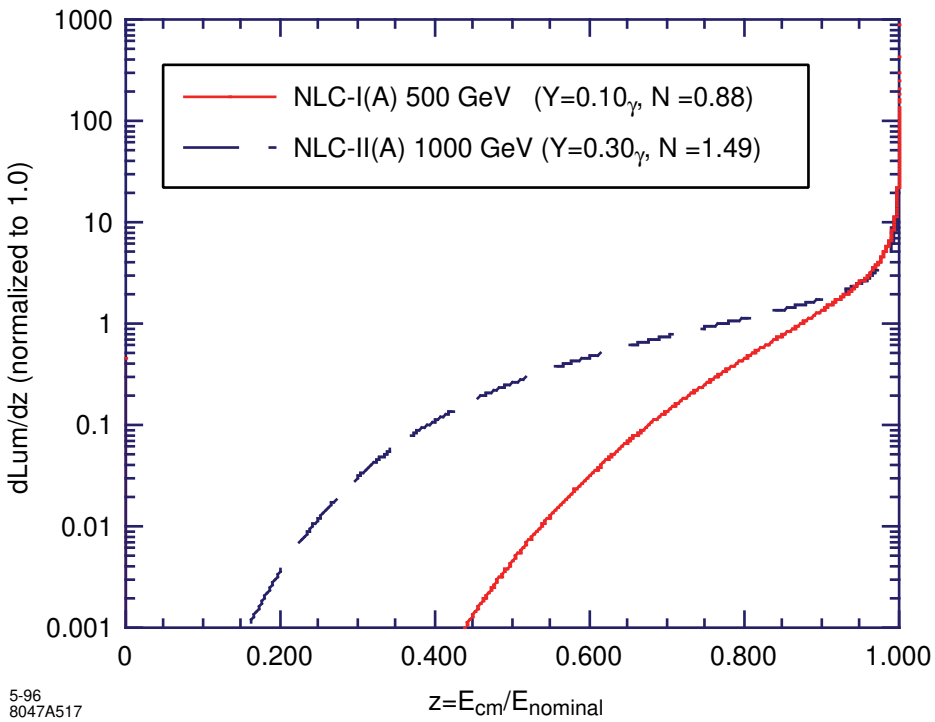

Figure 12-5. *A comparison of the beamstrahlung spectra for case A of the 500-GeV and 1-TeV machines.*

	500 GeV			1 TeV		
	A	B	C	A	B	C
Υ	0.112	0.0924	0.0878	0.334	0.296	0.289
N_γ	0.973	1.017	1.162	1.654	1.781	1.745
δ_b	3.55%	3.21%	3.52%	12.6%	12.6%	12.2%
R.M.S. e^+e^- c.m. energy spread	7.17%	6.44%	6.62%	15.9%	15.5%	15.2%
% of $\mathcal{L}$ within 0% of $\sqrt{s}_{\rm nom}$	40.9%	39.4%	35.0%	23.9%	21.8%	22.4%
% of $\mathcal{L}$ within 0.1% of $\sqrt{s}_{\rm nom}$	48.1%	47.0%	42.7%	28.6%	26.4%	27.2%
% of $\mathcal{L}$ within 0.5% of $\sqrt{s}_{\rm nom}$	54.5%	54.0%	50.0%	33.1%	31.0%	31.8%
% of $\mathcal{L}$ within 1% of $\sqrt{s}_{\rm nom}$	59.0%	58.8%	55.0%	36.3%	34.2%	35.1%
% of $\mathcal{L}$ within 5% of $\sqrt{s}_{\rm nom}$	75.6%	76.8%	74.4%	49.8%	48.1%	49.2%
% of $\mathcal{L}$ within 10% of $\sqrt{s}_{\rm nom}$	85.6%	87.2%	85.9%	60.2%	59.1%	60.1%
% of $\mathcal{L}$ within 100% of $\sqrt{s}_{\rm nom}$	100.0%	100.0%	100.0%	100.0%	100.0%	100.0%

Table 12-3. *Summary of quantities parameterizing the effect of beamstrahlung on the luminosity spectrum.*

is calculable and small, it should be comparatively easy to unfold from the data. Comparing Tables 12-2 and 12-3 we find that at 500 GeV all three parameter set choices result in smearing below the level expected from ISR. At 1 TeV, there is roughly twice as much smearing as that from ISR.

12.2.4 Measurement of the Luminosity Spectrum

The significance of the luminosity smearing depends on the physics channel under study. For discovery physics, some measure such as the fraction of the luminosity with $\sqrt{s} > 90\%$ of nominal is probably the best figure of merit. However, attention is generally focused on the region within 1% of the nominal energy, as it is critical for an excellent determination of the top quark mass. D. Miller has argued [Frary] that the measurement of the top quark mass will require machine parameters that result in very little smearing and that the detector have excellent forward tracking so as to use the collinearity distribution of Bhabha events to unfold the luminosity spectrum.

In Figure 12-6, we show the cross section for $t\bar{t}$ production as a function of nominal center-of-mass energy for $m_t = 180$ GeV/c^2. The theoretical cross section, indicated as curve (a), is based on the results of Peskin and Strassler [Peskin, 1991] with $\alpha_s(M_Z^2) = 0.12$, infinite Higgs mass, and nominal Standard Model couplings. Each energy-smearing mechanism, initial-state radiation (b), beamstrahlung (c), and beam energy spread (d), has been successively applied. Hence, curve (d) includes all effects.

A comment on the beam energy spread is in order. The expected shape of the single-beam energy spread is given in Figure 12-1. The luminosity-weighted center-of-mass energy spread, $\Delta E_{\rm cm}/E_{\rm cm}$, is calculated from the single-beam distribution given its dependence on the bunch spatial distribution, as discussed in Chapter 4. The resulting center-of-mass energy distribution is given in Figure 12-7, where the calculation has been simplified by ignoring variations in energy in transverse space. In this case, the input single-beam energy spread has FWHM of 0.8%, corresponding to the distribution shown in Figure 12-1. The resulting distribution in $\Delta E_{\rm cm}/E_{\rm cm}$ is strongly peaked at zero with an rms of 0.38%, as indicated in the Figure 12-1. It is expected that the single-beam energy spread can be comfortably adjusted within the FWHM interval 0.6% to 1.0%. For the top threshold, it is clear that the smaller width is preferred, and curve (d) of Figure 12-6 was calculated using the 0.6% width. The large top mass of about 180 GeV/c^2 presents a relatively broad,

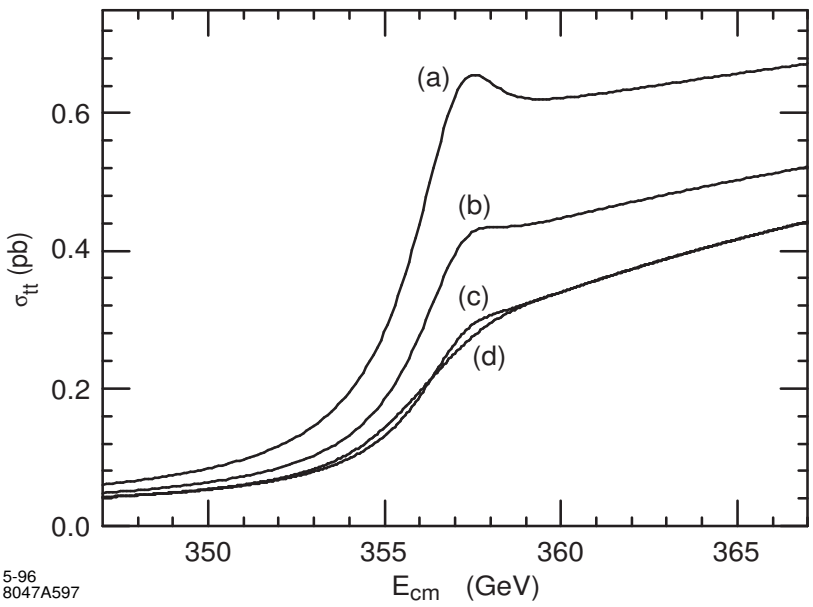

Figure 12-6. *Production cross section for top quark pairs near threshold for $m_t = 180\,\mathrm{GeV}/c^2$. The theoretical cross section is given by curve (a), to which the energy re-distribution effects have been applied. Curve (b): ISR; curve (c): ISR and beamstrahlung; curve (d): ISR, beamstrahlung, and beam energy spread.*

featureless threshold shape which is not nearly as sensitive to the $\Delta E_{\mathrm{cm}}/E_{\mathrm{cm}}$ distribution as would be expected if the top mass were smaller. Figure 12-8 shows the change in shape of the threshold cross section as the single-beam energy spread is increased.

12.3 Detector Background Sources

12.3.1 Beamstrahlung-produced e^+e^- Pairs

As the beamstrahlung photons travel in the high-field region of the opposing bunch, they can produce e^+e^- pairs. If deflected to large enough angles, the pairs can enter the detector and cause unwanted backgrounds. The probability for pair production is set by the Υ parameter. When $\Upsilon \geq\sim 0.3$ the pairs are coherently produced; that is, the virtual electron-positron pairs accompanying the beamstrahlung photon can exchange energy-momentum with the strong electromagnetic field and be kicked on-shell. When $\Upsilon \leq\sim 0.3$ the incoherent pair creation processes become dominant. In these, the e^+e^- pairs are created from individual scattering of real beamstrahlung photons through the Breit-Wheeler ($\gamma\gamma \rightarrow e^+e^-$) and Bethe-Heitler ($e^{\pm}\gamma \rightarrow e^{\pm}e^+e^-$) processes, and from the scattering of virtual photons through the Landau-Lifshitz ($e^+e^- \rightarrow e^+e^-e^+e^-$) process.

This phenomenon is dealt with in two ways. Most importantly, as long as $\Upsilon \leq\sim 0.3$ the number of coherently produced pairs per bunch crossing is negligible. This has been a design constraint of all colliders to date and seems reasonably easy to achieve at the start up energy of 500 GeV. Note the values of Υ listed in

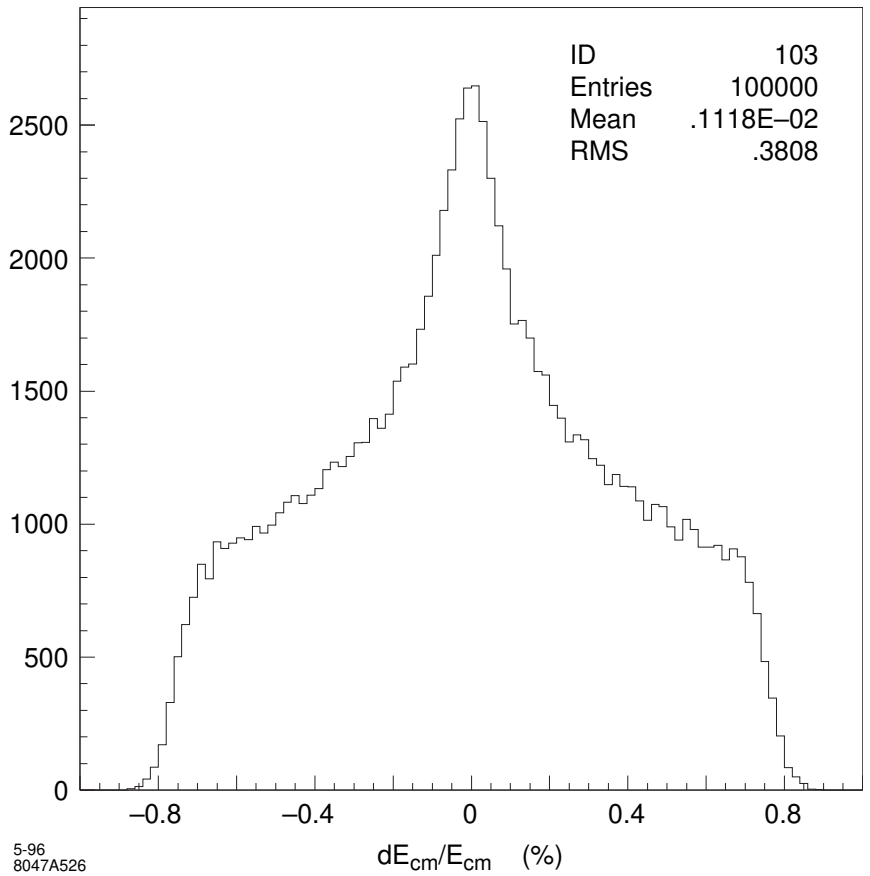

Figure 12-7. *Distribution of the center-of-mass energy, $\Delta E_{\rm cm}/E_{cm}$, due to the convolution of single-beam energy spread distributions for the two beams. The single-beam energy spread in this case has a FWHM of 0.8%, corresponding to the distribution given in Figure 12-1.*

Table 12-3 for the various collider designs. Figure 12-9 plots the contributions from each of the sources of pair production per bunch crossing versus Υ. Table 12-4 lists the number of pairs produced for the different parameter lists at 500 GeV and 1 TeV.

The preceding chapter introduced the ABEL Monte Carlo program used to simulate the beam–beam interaction. The ABEL program divides each bunch longitudinally, produces beamstrahlung photons and e^+e^- pairs as the bunches overlap, and propagates the particles through the high fields of the bunch overlap region. Figure 12-9 and Table 12-4 are calculated using the parameterizations of ABEL described in Ref. [Chen, 1990]. In the last run of experiment E144 at the SLAC FFTB, values of $\Upsilon \sim 0.25$ were reached. Coherent pairs were observed at about the level predicted by the ABEL simulation. In its upcoming run, E144 should probe the region of $\Upsilon \sim 0.5$–0.6. This experimental confirmation of the background level anchors the estimates of detector hit densities arising as a result of pair creation which is discussed in later sections of this chapter.

Secondly, a masking scheme can be designed which, in conjunction with the detector's solenoidal field, protects the detector from the majority of the deflected pairs. The mask takes the form of a truncated cone which begins about 0.5 m from the interaction point and has an opening angle determined by the maximum

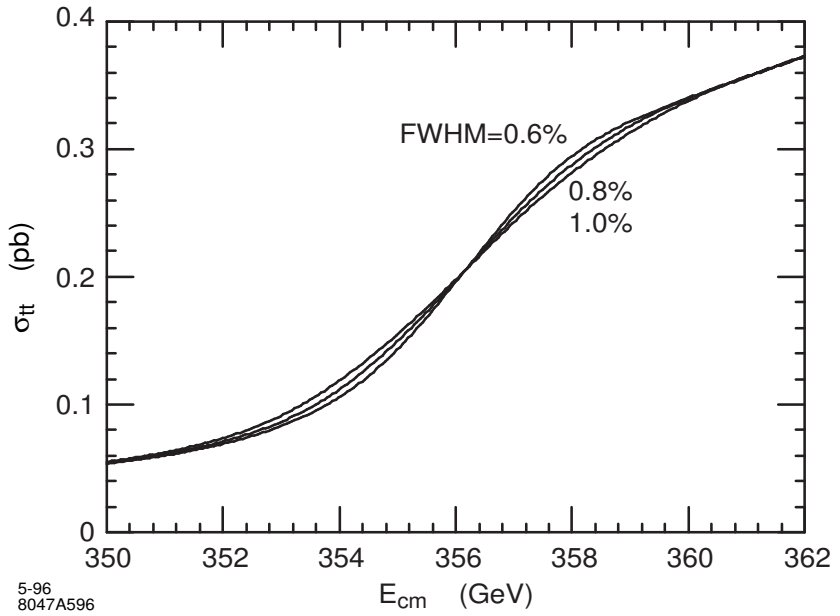

Figure 12-8. *Comparison of $t\bar{t}$ threshold shape, with all effects included, for different single-beam energy spreads. The three curves correspond to single-beam energy spread distributions with FWHM of 0.6%, 0.8%, and 1.0%, as indicated.*

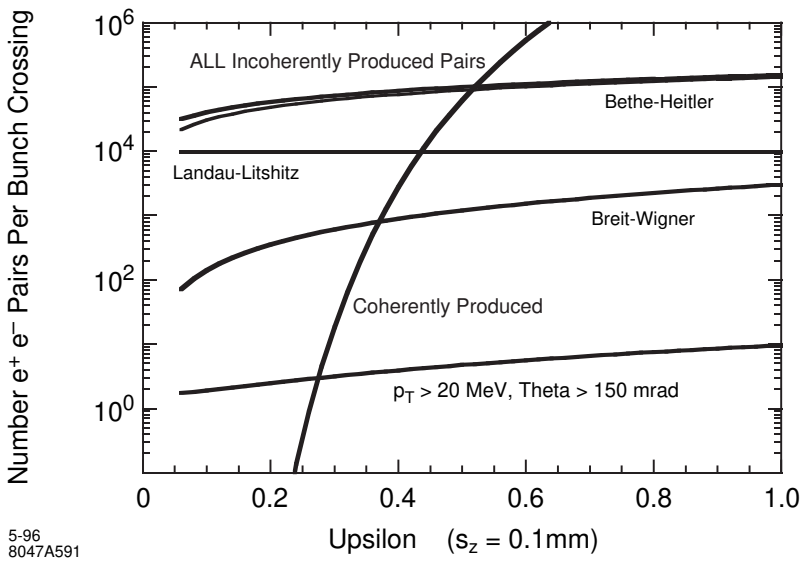

Figure 12-9. *Relative contribution of pairs from all sources as a function of Υ.*

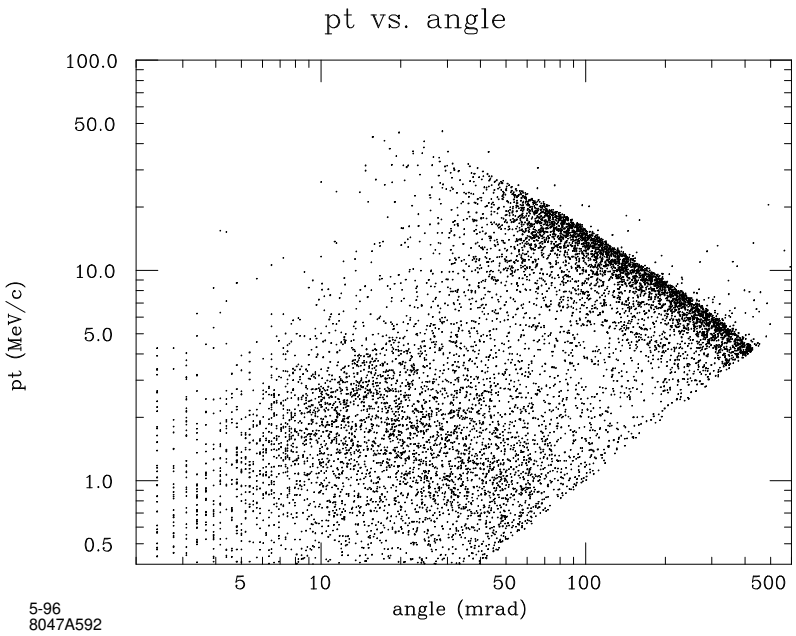

Figure 12-10. *p_t vs. θ distribution for pairs.*

kick the pair can receive from the field of the opposing beam. It defines a "deadcone" within which the detector is blind.

In coherent production, the pairs are not produced with significant intrinsic p_t; rather, roughly speaking, the e^+e^- are deflected by an angle proportional to $\sqrt{D_x/\epsilon} * \sigma_x/\sigma_z$, where D_x is the disruption parameter, ϵ is the ratio of the electron or positron momentum relative to the beam momentum, and σ_x and σ_z are the x and z beam spot sizes. The incoherent pairs have a more uniform energy distribution than the coherent process and can result in more particles with p_t and scattering angle θ outside the dead cone.

The pair partner with the same sign as that of the bunch that produced it will tend to oscillate within the field of the oppositely charged opposing beam. In the flat beam designs under consideration, there will be more oscillations in the vertical plane than the horizontal plane. The vertical oscillations will tend to cancel and the exit angle of the particle will be predominately in the horizontal plane. The oppositely charged member of the pair will see a defocusing force from the opposing beam and be quickly deflected out of the beam. From outside the beam, it sees the field of an elliptic cylinder charge distribution; up to terms of order $\log(D_x/\epsilon)$ the result for the maximum scattering angle is the same as that for the same-sign particle, although in this case the deflection angles in both the x and y planes are comparable.

Figure 12-10 shows the scatter plot of transverse momentum and scattering angle of the pairs generated by ABEL. The simulation used a 10-MeV cut on pair-member energy and a 2-mr cut on angle. The two bands seen in the plot corresponds to the opposite sign partners in the higher p_t region and the same sign partners in the lower p_t region.

	500 GeV			1 TeV		
	A	B	C	A	B	C
Detector dead-cone (mrad)	83	80	79	95	94	100
e^+e^- pairs per bunch X from coherent production	2.6E-13	1.4E-17	9.9E-19	76	13	9.1
e^+e^- pairs per bunch X from incoherent production	16.4E3	16.9E3	17.2E3	57E3	59E3	57E3
$N_{beamstr-e^\pm}$/bunch $\theta > 150$ mr, p_T >20 MeV	2.1	2.1	2.4	6.8	7.4	7.1

Table 12-4. *Summary of quantities parameterizing the backgrounds, before they interact in the detector.*

The particles travel in a helix from the IP. The solenoidal B-field strength and the distance of the conical mask from the IP determine the maximum particle momentum, and thus ϵ, that needs to be considered. All particles with lower momenta will curl up inside the cone. The maximum deflection angle can then be calculated from the formula alluded to above and the required radius of the conical mask determined. The dead cone is on the order of 100 mr and is tabulated for the various machine designs in Table 12-4. The thickness of the mask must be determined by detailed EGS or GEANT simulations to be adequate to stop the debris of the interacting electrons and positrons. Typically, the angle defining the outer dimension of the mask is 150–200 mr. Table 12-4 tabulates, for each of the parameter sets, the number of particles with p_t and θ large enough so that they fall outside the mask and hit the detector. Dealing with these particles depends on the time or bunch structure of the machine and on the timing capabilities of the detector.

12.3.2 Hadronic Backgrounds from $\gamma\gamma$ Interactions

In addition to the electromagnetic processes discussed above, the beamstrahlung photons can interact to produce hadrons and jets of hadrons. By folding the beamstrahlung spectrum into cross section estimates using an equivalent photon approximation, these hadronic rates can be estimated.

Hadronic events produced by beamstrahlung $\gamma\gamma$ annihilation are expected to be benign. Most of the hadronic events are minimum-bias events with small transverse momentum and small center-of-mass energy. Furthermore, the two photons involved in the collision usually have very different energies so that the hadronic system is highly boosted along the beam direction. Monte Carlo studies have demonstrated that the mean energy deposited in a detector from an hadronic background event will be 8 and 11 GeV for colliders with $\sqrt{s}$=500 and 1000 GeV, respectively. Here it is assumed that the detector has typical electromagnetic and hadronic calorimetry over all solid angle with the exception of a hole (dead cone) with $|\cos\theta| > 0.985$. The energy deposition with a larger solid angle dead cone of $|\cos\theta| > 0.900$ will be 3.3 GeV and 4.4 GeV for $\sqrt{s}$=500 and 1000 GeV, respectively.

12.3.3 Quadrupole and Bend Synchrotron Radiation

Linear collider designs obtain a small beam spot at the IP by using strong focusing magnetic quadrupole lenses close to the IP. SR generated by particles passing through these quadrupoles and bend magnets in the final focus is a potential source of background in the detector. SR backgrounds in the SLD detector at the SLAC Linear Collider (SLC) are in reasonable agreement with calculations. The SLD/SLC model implies that the nominal Gaussian beam core generates a small SR background in the final "soft" bend magnet, and negligible SR background in the quadrupoles. However, the non-Gaussian beam tail or beam halo can result

in significant background due to synchrotron radiation generated in the quadrupoles (QSR). This source is controlled by collimation of the beam and by limiting the angular divergence at the IP. The QSR background is quite variable, and measures that control it can reduce luminosity.

Apertures in the beam line near the IP are matched to the design angular divergence and collimation. The SLD has a carefully designed set of internal masks to limit the SR background in the detector, especially the drift chamber. The SR background at SLD is reasonably well modeled by a nominal Gaussian core and a beam tail at the IP that is a very broad Gaussian containing 1% of the nominal charge. This "1% flat tail" is purely arbitrary and difficult to measure directly. The SR background generated by the tail depends directly on the fraction of the beam it contains and how it is collimated.

SR backgrounds in the SLD were modeled with EGS4, starting with SR photon fluxes calculated with a modified version of QSRAD. QSRAD was written to study SR generated by the PEP-I beam in the last two quadrupoles prior to the IP. The program traces weighted rays from a Gaussian beam profile through the specified magnetic optics and produces a geometric fan of synchrotron radiation with uniform power density and constant critical energy for each magnetic element. These fans are then traced, and a tally is made of the fraction of each fan that strikes opaque surfaces with specified apertures. The distribution of photon critical energies is accumulated for each surface and converted to a photon energy distribution. The code provides additional information to characterize the SR photons incident on each surface, and this is the input data for an EGS4 model of the masking and detector.

At SLD the SR due to the final soft bend has a critical energy of 70 keV and results in 7×10^8 photons per pulse incident on a mask 1.3-m down beam from the IP. This is $\approx 1.5 \times 10^{10}$ keV per pulse at 120 Hz. EGS4 calculations predict that this would result in 280 photons entering the SLD drift chamber per pulse. This corresponds to about 0.5% wire occupancy. The major component of SLD background from quadrupoles in the model is due to photons striking the same mask. There are 1.5×10^8 photons per pulse with a critical energy of 1 MeV. This is about 5×10^{10} keV per pulse and, according to EGS4, results in 73 photons in the drift chamber. However, this background, due to the tail, is very sensitive to the model, and can be made considerably larger by varying the assumptions about the IP divergence angle and the beam collimation, thereby introducing new sources. We believe that variations in these parameters contribute to the fluctions in backgrounds actually observed. The energy spectra for the NLC calculation contain far more SR energy than calculated for the SLD case. The spectra in Figure 12-11 correspond to a critical energy of 200 keV and contain between 1.2×10^{11} keV and 1.5×10^{11} keV per train of 90 bunches.

Preliminary calculations of NLC synchrotron radiation have been performed for the 1-TeV machine with 500-GeV beams using the currently available final focus optics [Helm, TLCFF28]. The QSRAD code has been enhanced to include bend magnets in addition to quadrupoles, and to allow SR from individual magnets to be turned on or off. Optical elements within 300 m of the IP have been included in the calculation. SR from more distant magnets cannot reach the IP region directly because of the bends centered at 183 and 261 m from the IP. The beam at the IP was taken to be 226 nm × 3.57 nm with angular divergence 22.6 μr × 28.6 μr, corresponding to the 1-TeV parameter set A of Table 12-1. Calculations were done for a single bunch containing 9.5×10^9 electrons, and, unless otherwise indicated, all results quoted here are for a single bunch. Collimation was modeled as perfect rectangular collimators at $7\sigma_x$ and $35\sigma_y$. SR from beam tails was calculated for an arbitrary 1% flat tail, 9.5×10^7 electrons per bunch uniformly distributed over the collimator aperture, and the reader can scale this up or down as desired. In reality, detector elements will integrate backgrounds over a bunch train, and the single-bunch numbers should be multiplied by 90 bunches per train for background considerations.

The first studies of SR in the NLC final focus lead to the relocation of the final bends and other modifications. In the current design the final bend ends 151 m from the IP, apertures in the final focus have been increased,

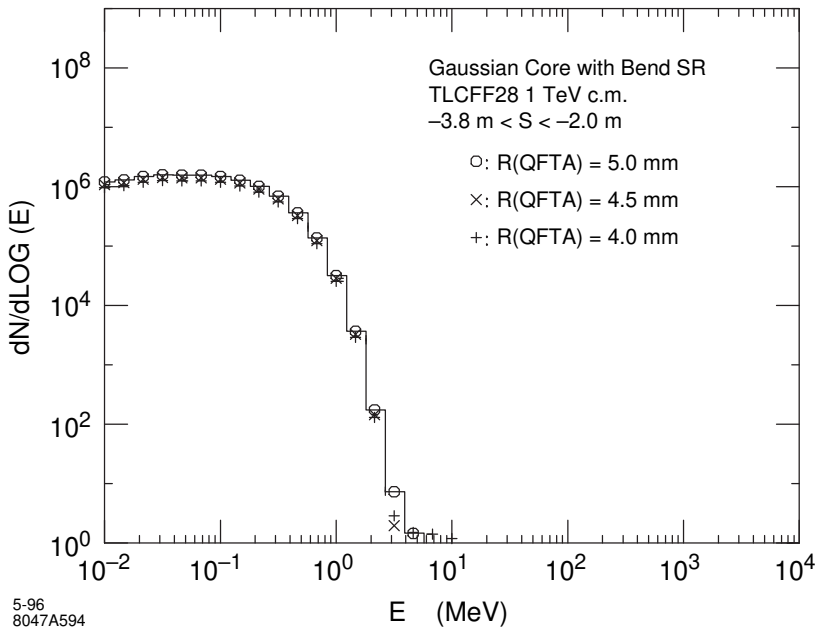

Figure 12-11. *Energy distribution of synchrotron radiation photons, from particles in the Gaussian core of the beam, striking the inner aperture of the QFTA quadrupole. There are only minor variations in the range of radii considered.*

and the quadrupole closest to the IP (QFTA), with the smallest aperture, is shorter than in the previous lattice.

Our experience with EGS4 simulations of SLD backgrounds and initial calculations of SR at the NLC indicate that the most serious source of SR background in this model of the NLC is likely to be the SR photons incident on the inner surface of the beam pipe through QFTA, the magnet closest to the IP. The calculations reported here are for this source only. We consider here the inside of a cylindrical surface of length 1.8 m, between 2.0 and 3.8 m from the IP. This includes the interior of QFTA and a mask that is likely to precede the magnet. The calculation is done for several quad apertures, as discussed below.

The Gaussian beam results in 1.2×10^7 photons above 10 keV energy incident on the inside of a cylindrical QFTA of 4.5-mm radius. These photons are all from the final "soft" bend (SBSR), and have a critical energy of 200 keV. The number of incident photons changes by only 10% if the radius of the magnet aperture is changed by 0.5 mm. The energy spectra are shown in Figure 12-11. These numbers are independent of assumptions about the beam, other than parameters that are well defined. Furthermore, the interior of QFTA can be shielded from the SBSR by a mask in the horizontal plane 40 m from the IP. The half-aperture of this mask would be 3 mm, about $10\sigma_x$, whereas the beam is collimated at $7\sigma_x$. Although the mask is required on only one side of the beam, it would be symmetric to minimize wakefield effects, which must still be evaluated before this mask is accepted as part of the design.

The effect of the tail is calculated without the SR from the bends, because that has been included with the Gaussian core. Results for the flat tail are very dependent on assumptions about collimation and the population of the beam tail. With the assumptions above, the 1% tail calculation results in 3.7×10^5 photons per bunch with an average energy of 5.3 MeV incident inside QFTA if the aperture is 4.5 mm in radius. This SR is all from QFT5 and QFT6, 134 m and 150 m from the IP.

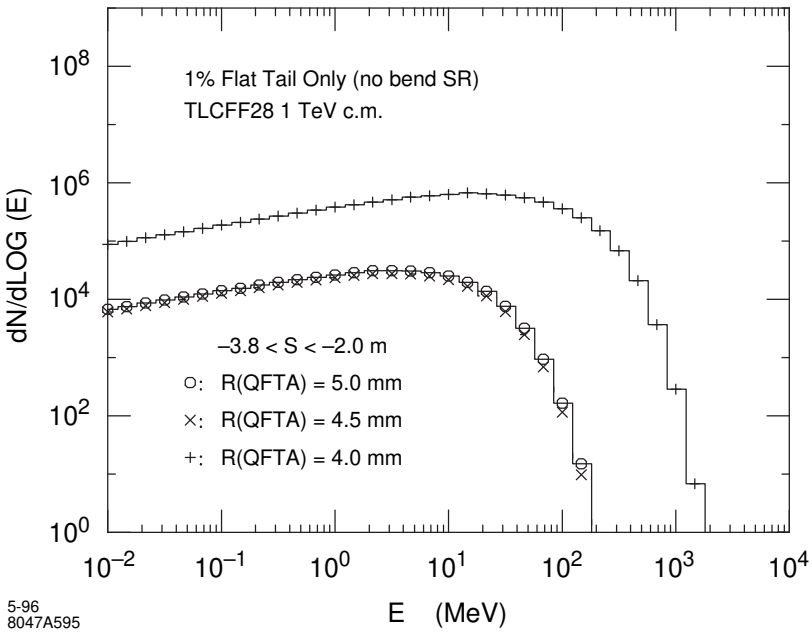

Figure 12-12. *Energy distribution of synchrotron radiation photons, from particles in the assumed 1% flat tail of the beam, striking the inner aperture of QFTA, the innermost quad. Photons produced by bends and photons produced by the Gaussian beam core are not included in this plot. The spectra for 5.0-mm and 4.5-mm radius do not differ significantly. When the aperture is small enough to intercept QSR from the superconducting quadrupoles the incident QSR is much larger, as shown for a 4.0-mm radius.*

There is also a large flux of 5.1×10^7 SR photons per bunch, incident where the aperture decreases between QFT1 and QFTA. Calculation shows that this can be reduced by an order of magnitude, shifting the flux upstream to a protection collimator 10 m from the IP. This SR is primarily in the vertical plane, and 90% can be intercepted by a 5-mm mask, which is large compared to the 2-mm $35\sigma_y$ beam envelope at this location.

If the radius of QFTA is increased to 5.0 mm, there is a small increase in the number and average energy of the incident photons. The energy spectra are shown in Figure 12-12. However, Figure 12-12 also shows that reduction of the radius to 4.0 mm results in a large increase in both the number and energy of the incident photons. The total SR energy incident on the inner bore of QFTA increases by more than two orders of magnitude. This is because the smaller aperture intercepts a large flux of energetic QSR generated by the beam tail in the superconducting quadrupoles QFT1 and QFT2. This must be considered as the design evolves, because the only way to compensate for a smaller QFTA aperture is with tighter vertical collimation. In this lattice the collumator aperture must be reduced by one σ_y to compensate for each 125-μm reduction in QFTA radius.

The exit aperture to the dump line across the IP will have to be larger than QFTA in order to avoid a large flux of QSR incident on the face of the first dump line quad. The non-zero beam crossing angle makes this possible. For a 4.5-mm radius QFTA the first dump line quad aperture should have a 7-mm radius. Figure 12-13 shows the $7\sigma_x$ and $35\sigma_y$ beam envelopes. In the figure the optical elements are subdivided and the SR fan produced by each element traced to the IP. It is clear that the SR fan in the vertical plane from the final doublet is what sets the exit aperture. The radiation that does hit QFTA is seen to come from Q6, approximately 150-m upstream of the IP.

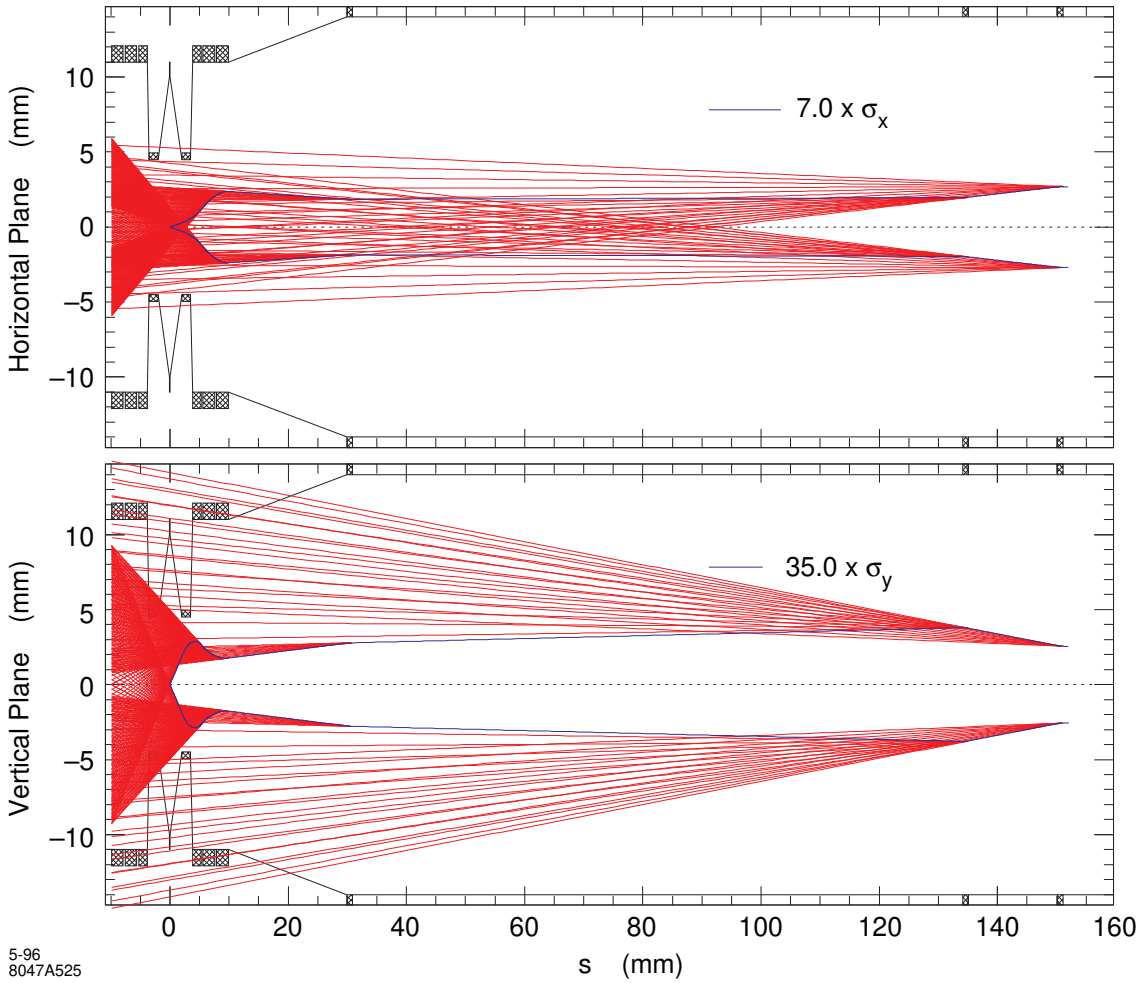

Figure 12-13. *The $7\sigma_x$ and $35\sigma_y$ beam envelopes and the SR fans emitted for the lattice used for these calculations.*

These studies should continue in conjunction with design of the final focus and the dump line. More detail must be included in the models of the apertures to identify those sources which are most likely to result in detector backgrounds. It is not obvious that the 1% flat tail assumption, which seems to work at the SLC, is reasonable for the the NLC. Because of its importance in estimating detector backgrounds, an effort should be made to estimate the likely beam halo at NLC.

The results of these SR calculations are used as input to EGS4 and GEANT models of a detector and its masking, and the first results are described later in this chapter. This study is far from complete, and detailed results from the EGS calculation will be used to propose further modification of the lattice and magnet apertures. The severity of the backgrounds modeled here may influence the choice of detector technology. The machine design has been able to incorporate suggestions motivated by the background calculations, and considerable progress has been made in reducing the potential for backgrounds due to synchrotron radiation.

12.3.4 Muon Backgrounds

The same collimators which limit beam phase space and protect the detector from SR backgrounds produce considerable numbers of muons as the incoming beam interacts with them, primarily through the Bethe-Heitler process $e^{\pm}N \rightarrow e^{\pm}\mu^{+}\mu^{-}N$. The problem was first encountered in 1988 with the Mark-II detector at the SLC. To quantitatively study the production and transport of the muons the program MUCARLO [Feldman] was written. It successfully reproduced the experimental results for the number and spatial distributions of muons hitting Mark-II. The backgrounds were reduced to acceptable levels by moving the primary collimation to a point at the end of the linac, approximately 1500-m from the IP and separated from the detector by the SLC arcs, and installing magnetized iron spoilers in the final focus tunnels. At the NLC, this philosophy is duplicated by locating the collimation section at the end of the linac, ~ 5.2-km from the interaction point, and placing the final focus in a tunnel section dug at 10 mr with respect to the linac, the "Big Bend."

In 1990, the MUCARLO program was modified [Keller, 1991] for use with beams of up to 250-GeV energy. Using the TRANSPORT deck for a 500-GeV-c.m. collider available in June 1990 (FFN09, R. Helm), the placement of five toroidal spoiler magnets was optimized to maximize the number of electrons that could hit a collimator before producing one muon that would make it to the detector.

In 1993, MUCARLO was again modified. Beams of energy up to 500 GeV were allowed, and muon production by direct e^{+} annihilation, $e^{+}e^{-}\rightarrow\mu^{+}\mu^{-}$, and photopion production, $\gamma A \rightarrow X\pi(\pi \rightarrow \mu\nu)$, were included. Using the TRANSPORT deck for a 1-TeV-c.m. collider available in June 1992 (TLCFFN5, R. Helm), the muon background study was repeated [Keller]. Most of the figures presented in this section are from that study. Figure 12-14 shows a schematic of the collimation and final focus beam transport sections being considered at that time. The collimation section has a series of six Hi-Z collimators and a total bend of 6.14 mr followed by a big bend with a total bend of 10 mr followed by the final focus with a reverse bend chromatic correction section of $\pm$2.21-mr bends. The model includes a 3.05-m-square cross section concrete tunnel through sandstone, concrete support girders under the beam elements, and dipoles and quadrupoles which include return flux in the iron and pole tips. The detector is assumed to have a 4.5-m-radius cross section centered on the IP. There is a series of magnetized iron spoilers of alternating polarity distributed through the final focus.

Figure 12-15 shows how the spoilers are arranged in the tunnel at a given location. The field in the iron was modeled using the two-dimensional program POISSON.[7] Each spoiler is 9.1-m long with a winding slot width and height of 3.2 cm and 126 cm, respectively. Each set of "tunnel-filler" spoilers weighs 750 tons and would cost \$2–3 million installed. For magnetized iron with a field of 16 kg, the ratio of bend angle to scattering angle is $\theta_{\rm bend}/\theta_{\rm MCS} \approx 3\sqrt{L}$, where L is the length of the spoiler in meters.

An alternative to large tunnel-filler magnetized iron spoilers has been proposed, consisting of nested iron cylinders with opposite-polarity azimuthal magnetic fields as shown in Figure 12-16. The idea is that the nested cylinders are located downstream from each muon source and are long enough to either range out muons or cause enough energy loss so that the muon is unlikely to reach the detector. A version of the nested cylinder idea was tried in MUCARLO, and the results are presented in Figure 12-17.

After the muon exits the source, the Monte Carlo program swims it in 30-cm steps through the tunnel. When material is encountered, the muon scatters, loses energy, and bends (if a magnetic field is present). The trajectory of each muon is followed until the muon either stops or reaches the IP. For the purposes of this study, the details of the detector, *e.g.,* trackers, calorimetors, and muon walls, are not included. A muon which reaches the IP within a radius of 4.5 m from the beam line is counted as a detector hit.

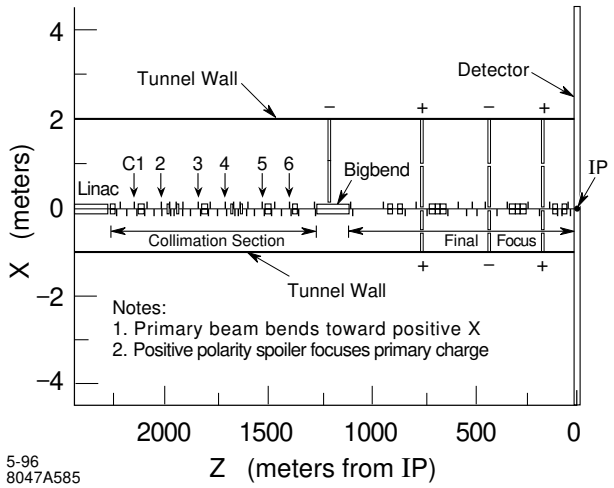

Figure 12-14. *Plan view of the 1992 NLC beam line in the tunnel with magnetized iron spoilers.*

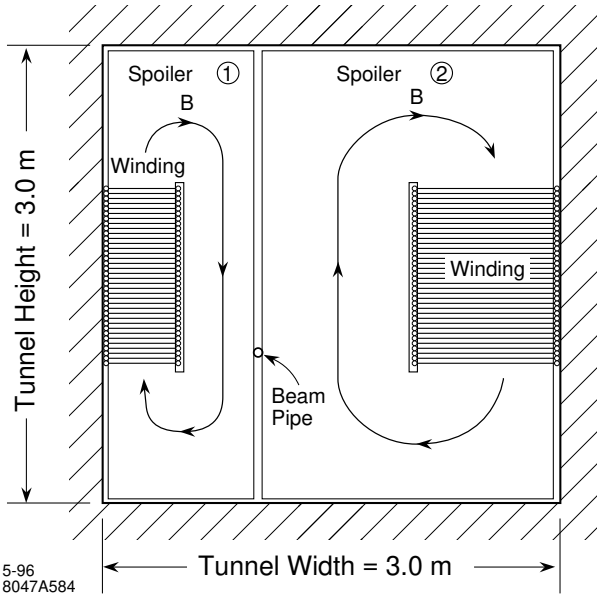

Figure 12-15. *Two side-by-side magnetized iron spoilers filling a 3 × 3-m beam tunnel.*

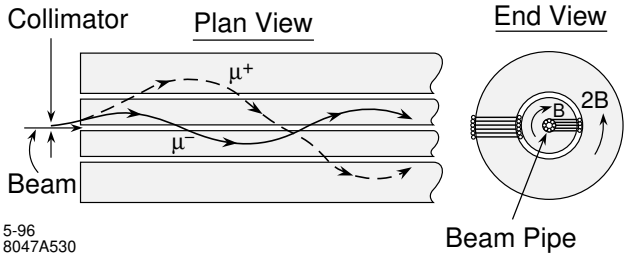

Figure 12-16. *Nested, magnetized iron cylinders of opposite polarity to channel both μ^+ and μ^-.*

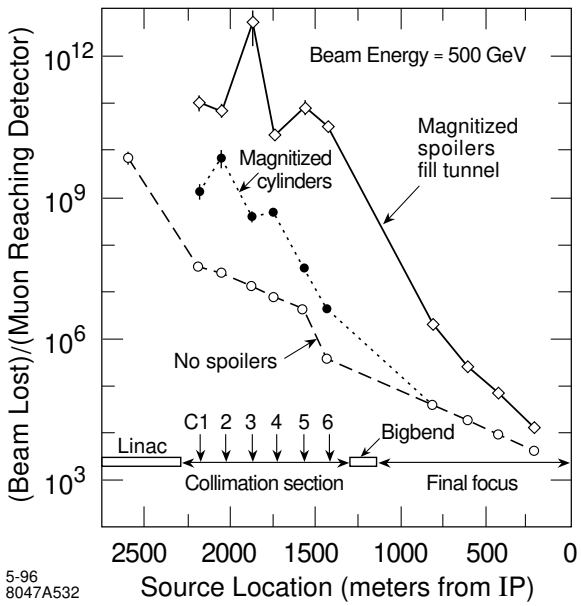

Figure 12-17. *Results of muon Monte Carlo calculations, based on the 2-km final-focus design of 1992, for three conditions: no spoilers, and two types of magnetized iron spoilers.*

Figure 12-17 shows the number of beam particles which must hit a collimator to produce one muon in the detector as a function of source location in the beam line. As a worst case, an e^+ beam was chosen for this study so that direct annihilation production could be included. The source points include the six Hi-Z collimators in the collimation section and collimators at four high-beta points in the final focus, which are potential scrapers of beam-gas coulomb scattering or beam-gas bremsstrahlung.

From the curve labeled "No spoilers" it is seen that a beam loss of 10^{10} per bunch train anywhere in the collimation section will result in a muon background which is many orders of magnitude away from the design goal. The curve labeled "Magnetized spoilers fill tunnel" in Figure 12-17 is the result of adding magnetized iron spoilers which fill the tunnel at three locations in the final focus and one magnetized iron piece in the tunnel aisle next to the 10 mr big bend. It is seen that for all six collimators in the collimation section, more than 10^{10} beam particles must be lost to produce one muon in the detector. This satisfies the design goal of allowing a 1% continuous beam loss in the collimation section.

The curve labeled "Magnetized cylinders" in Figure 12-17 shows the results of filling all drift spaces in the collimation section with magnetized iron cylinders described above. The result is considerably worse than for magnetized iron spoilers which fill the tunnel and does not meet the design goal. This is because the magnetized cylinders must be interrupted by beam elements, especially dipoles in the chromatic correction sections, which disperse muons away from the cylinders and therefore disrupt the channeling orbits.

For the case of the magnetized iron tunnel-fillers, Figure 12-18 shows histograms of muon-production momenta and final momenta for muons which hit the detector from the six sources in the collimation section. It is seen that the initial muon momentum must be greater than 300 GeV/c to hit the detector from sources outboard of the big bend. Figure 12-19 shows the spatial distribution of muons from the collimation section which reach the IP. It is seen that increasing the detector dimensions by 2–3 m in the horizontal direction would intercept significantly more muons.

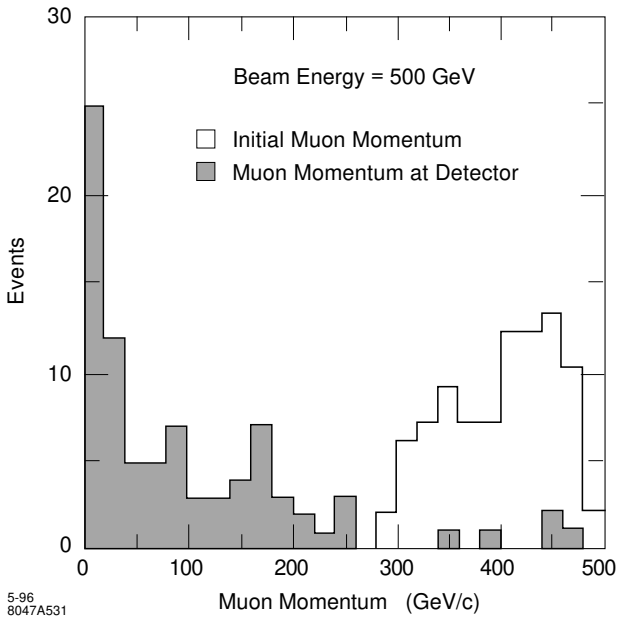

Figure 12-18. *Momentum distribution of muons which hit the detector from six sources in the collimation section. The normalization is arbitrary.*

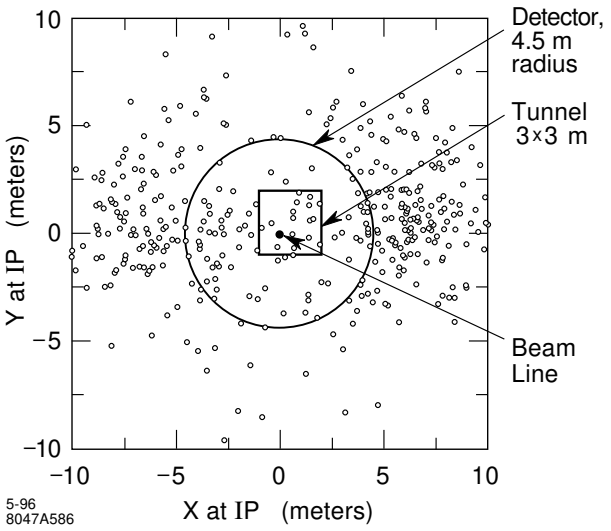

Figure 12-19. *Spatial distribution of muons which reach the IP from six sources in the collimation section. The normalization is arbitrary.*

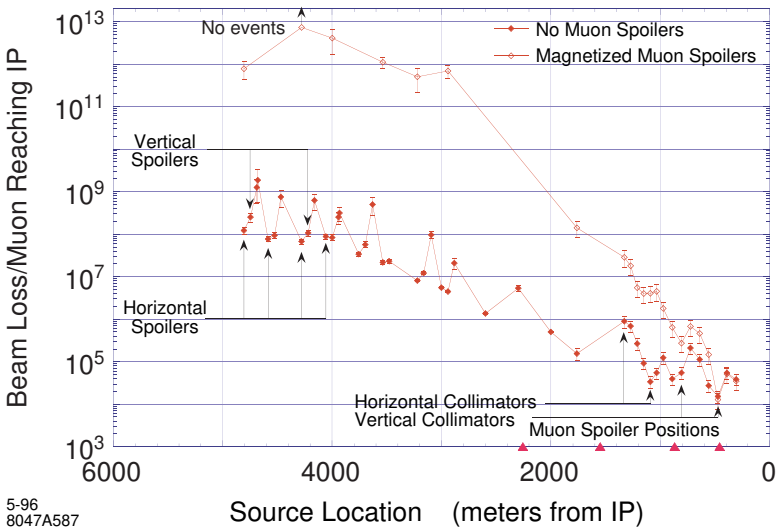

Figure 12-20. *Results of muon Monte Carlo calculations updated for the collimation and final focus design available in early 1996. Data are presented for calculations with and without a muon spoiler system. The data from the previous calculation (Figure 12-17) are also plotted for reference.*

For sources in the collimation section of a 1-TeV center-of-mass linear collider, a system of magnetized iron spoilers which fills the tunnel and meets the design goal of allowing a continuous 1% beam loss, or 10^{10} beam particles per bunch train, was found. This is more than a three orders of magnitude improvement over the case with no muon spoilers. For the case of magnetized iron cylinders which fill all drift spaces in the collimation section, the design goal was not met.

These studies were recently repeated using the current design for the collimation section, big bend, and final focus (TLCBD01B, R Helm). While the tunnel size, magnet design, and magnet support are important inputs to the program, we still assume the original 3×3-m-square tunnel cross section and SLC-like magnet and support. Figure 12-20 shows the results for two configurations: no spoilers and with tunnel filling magnetized spoilers. It can be seen that the newer design, with its longer beamline, allows for a larger number of beam particles to be lost per muon arriving in the experimental hall. Nonetheless, muon spoilers are still required to attain the design goal. The spoiler locations used here were determined by scaling those of the older, shorter final focus design. Additional optimization of the spoiler system is in progress.

12.4 Detector Issues

There has been much less thought devoted to the NLC detector than to the accelerator itself. In physics studies conducted in Japan and Europe, the detector is envisioned to follow the solenoidal architecture typified by OPAL, ALEPH, or SLD, scaled appropriately for the increase in center-of-mass energy and having, depending on the study, improved tracking, vertexing, or calorimetry. Table 12-5 gives a list of possible physics-motivated specifications as summarized in a recent review.[TRC 1995]

Two issues appear to drive the conceptual design of the detector: the required momentum resolution of the charged particle tracking system and the requirements for "special" support systems for controlling vibrations of the final focus. A pixel vertex detector (presumably CCDs), a moderate resolution electromagnetic and hadronic calorimeter, and a muon identifier of instrumented steel plates are non-controversial.

Recently, a "straw-man detector" design has been presented [SLAC 1996] which is based on a compact five-layer tracking system using double-sided 5-μm-resolution silicon strips in 4T magnetic field. Such a system would have a momentum resolution around 0.03%×P(GeV), and would be resistant to the expected backgrounds and instabilities of the NLC. By keeping the coil inside the electromagnetic calorimeter it remains relatively thin (2–3 radiation lengths) and short (2–3-m in length). Figure 12-21 shows a quadrant this detector.

The nominal nanometer vertical size of the NLC focus drives the question of the quadrupole support system. The design possibilities include a rolling support of the quadrupole from a retractable end door such as in the SLD; a static steel end door supporting the quadrupole with retractable muon system and calorimeter for interior access; and actual intrusion of a static steel and concrete buttress into the door region for quadrupole support. Measurements of the differential motion of the quadrupole end of SLD have been made (see Section 12.4.5). It appears that, with appropriate care, seismic concerns will not overly compromise the detector design.

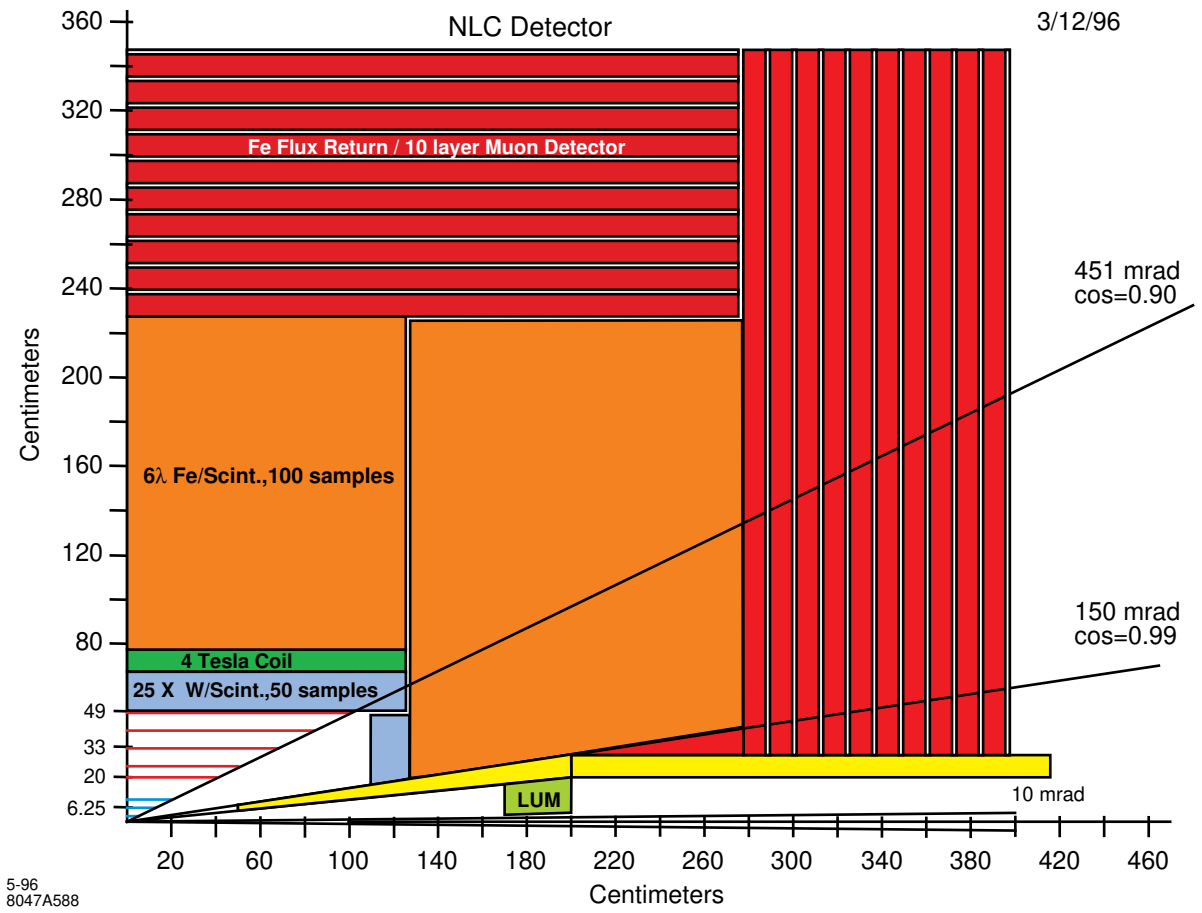

Figure 12-21. *A compact NLC Detector, robust against backgrounds. The scale is in cm.*

12.4.1 Effect of Backgrounds on the Detector

The zeroth-order masking design for the IP is shown in Figure 12-22. This geometry has been programmed into EGS4, and full simulations of the effects of the interactions of beamstrahlung-produced pairs, QSR-produced photons, and lost beam particles are in progress. Tungsten is used for Mask M1, M2 and the luminosity monitor. The beam pipe made of 750-μm-thick beryllium is located at $r = 1$ cm near the IP and of 500-μm-thick stainless steel for the rest. The beam pipe is pulled back to a larger radius as soon as it is past the maximum z required by the vertex detector. The rf shield made of 200-μm-thick copper is necessary to avoid the wakefield effect. The solenoid field in the detector and the quadrupole field in the final quads are included, and charged particles are transported properly in the magnetic field. However, non-axial field components of the solenoid or fringing field of the quads are not considered. The vertex detector is modeled with four layers of sillicon+beryllium at the radii of 1.2, 2.7, 3.8, and 4.8 cm with an angular acceptance of $|\cos\theta| < 0.9$. The layer thickness and the locations of the outer three layers are chosen after the new SLD vertex detector. In addition to the vertex detector layers, there are massless scoring planes at $r = 10$, 15, 20, 25, and 30 cm with $|\cos\theta| < 0.9$. The tracking chamber is located at $r = 30$ cm and $|z| < 100$ cm.

	LEP/SLC-Style	ee500 1991	ee500 Typical	JLC Detector	1 TeV Detector	Units
Tracking $\frac{\delta p_t}{p_t{}^2} = C$						
$C =$	8	5-100	10	1	2	$\times 10^{-4}$ gev/c^{-1}
E-M Calorimeter						
$\frac{\delta E}{\sqrt{E}} =$	0.2	0.02-0.15	0.1	0.15	0.10	$\sqrt{\text{GeV}}$
Hadronic Calorimeter						
$\frac{\delta E}{\sqrt{E}} =$	0.9	0.3-1.0	0.8	0.40	0.65	$\sqrt{\text{GeV}}$
Energy Flow						
$\frac{\delta E}{\sqrt{E}} =$	0.65	0.3-0.8	0.5	0.3	0.4	$\sqrt{\text{GeV}}$
Vertexing $\delta(IP) = A \bigoplus \frac{B}{p}$						
$A =$	25	5-20	10	11	10	μm
$B =$	100	50-100	50	28	50	μm GeV/c
Hermetic coverage						
$\lvert\cos\theta\rvert <$	0.96	0.70-0.99	0.95	0.98	0.98	

Table 12-5. *Examples of detector performances used in physics studies.*

The complete history of secondary electrons, positrons, and photons produced from the incident e^+e^- pairs and synchrotron photons was traced using EGS, and the background level in the detector was calculated.

The figure of merit we have traditionally used for the maximum allowable background level is one charged particle hit/ mm^2/train-crossing for a pixel-based vertex detector, and 10,000 photons/train-crossing for a drift chamber.

This work has resulted in changes to the final-focus lattice and to the design of the final quadrupole doublet. The process has been iterative and is still in progress; the reader is warned not to assume that we have presented a unified and consistent set of results throughout the relevant sections of the design report.

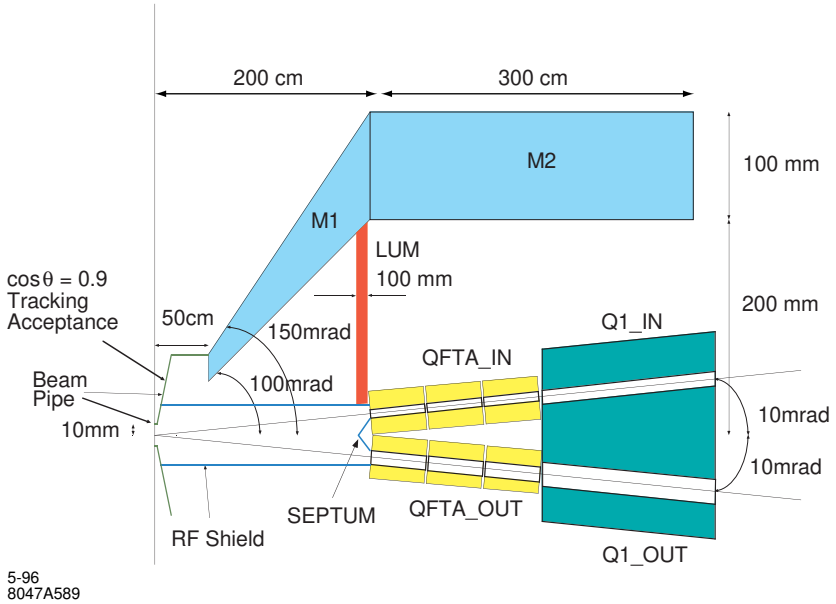

Figure 12-22. *First pass at NLC masking:*

M1 Mask	Tapered Tungsten Cone beginning at z=0.5 m and ending at z=2.0 m, with inner and outer angles of 100 and 150 mr, respectively.
M2 Mask	Tungsten annulus with 10-cm wall and inner radius 20 cm, $2.0 < z < 5.0$ m.
QFTA_IN/OUT	Incoming/Outgoing Sm2Co17 FF quads rotated 10 mr in x–z plane. QFTA_IN - Inner/Outer radii = 4.5/20.0 mm QFTA_OUT - Inner/Outer radii = 7.5/20.0 mm Longitudinally divided into three 5.0-cm-long segments with 2.0-cm gaps. L^* = line at 10 mr to IP is 2.0-m long.
Q1_IN/OUT	Superconducting magnet with Q1_IN aperture = 5 mm; Q1_OUT aperture = 8 mm. Extends from 3.5 to 5.0 m.
Beam Pipe	750-μm Be beam pipe with 100-μm Titanium liner at 1.0 cm, at $z \pm 2.1$ cm, which is joined onto a 500-μm Stainless sectioned flared at 451 mr until r = 7.56 cm, after which it proceeds to the M1 mask and follows its inner contour.
RF Shield	200-μm Cu extension at r = 2.75 cm, z = 2.1 cm, extending at constant radius to z = 165 cm, then proceeding via two "legs" to join electroplated inner radius of in-/out-going quads.
SEPTUM	200-μm Cu cone beginning at z = 189 cm and proceeding to z = 2.0 m at an angle θ, where $\theta = \arctan((20\text{ mm} - 7.5\text{ mm})/11\text{ cm})$.
LUM	10-cm Tungsten with back end at 195 cm, outer radius tapered at 150 mr at M1, inner radius tapered at 10 mr at radius of outgoing quad.

Beamstrahlung-produced pairs

The ABEL simulations of the beam-beam interaction have been described in the final-focus chapter (Chapter 11) of this report. We have concentrated on the data set which describes the 1-TeV NLC parameter set A machine design listed in Table 12-1. The simulations used a 10-MeV cut on pair-member energy. This cut is responsible for the hard edge at the lower right corner of Figure 12-10. As the bremsstrahlung probability for high-Z materials is not negligible at 10 MeV, the cutoff energy should be lowered to 1 MeV in ABEL. The effect of lowering this cut is under study.

Particles with a large p_t will hit the vertex detector directly, while particles with a small p_t will traverse the detector following the axial magnetic field and hit the final quad face producing secondary charged particles which come back to the IP and hit the vertex detector. Figure 12-23 shows the average hit densities of e^+e^- per train at $r = 1$ and 2 cm as a function of z for two solenoid field strengths. The solid histogram represents the particles directly hitting the layer, while the dashed histogram is for the backscattered particles. Since the interaction of e^+e^- at a few MeV is very dependent on the detailed geometry and materials, the calculation presented in Figure 12-23 used massless scoring planes at r=1 and 2 cm. Since no interactions were simulated at these layers, one particle could contribute multiple hits. Therefore, the numbers should be considerd as an upper-limit. With this caveat, the hit density of directly hitting particles is about 2–3/mm^2/train at r = 1 cm and less than 1/mm^2/train at r = 2 cm; an acceptable level for a pixel-based vertex detector. The hit density of backscattered particles is, however, about ten times higher. Low Z coatings on the quadrupole and luminosity monitor faces will substantially reduce the flux of soft backscattered particles. Improvements to the IR layout and masking to reduce the backscattering probability are underway.

This study has tried to find the minimum feasible radius for a vertex detector. The reader must remember that at r = 3 cm, the direct pair background is essentially zero in a 4-T field. Furthermore, at 500 GeV-center-of-mass, backgrounds are down by another factor of 4.

Figure 12-24 shows the number of photons per train striking a scoring plane at r = 30 cm, the nominal position of the inner wall of a central tracking chamber as a function of the solenoidal field of the detector. The number of electrons crossing the scoring plane is negligible. Since the majority of photons are produced by the interactions of pairs at the Mask M1 face and at the rf shield, the background can be reduced substantially by using higher solenidal field strength so that more pairs are curled up within the deadcone. However, even at 4 T, the total number of photons is 80K/train, which may not be tolerable for a drift chamber.

Figure 12-25 shows the number of photons per mm^2 per train striking the vertex detector layers and scoring planes from r = 1.2 cm to r = 30 cm for three solenoid fields of 2, 3, and 4 T. These hit densities can be used to optimize the position of a vertex detector or intermediate tracker. As Figure 12-25 shows, 10/ mm^2 as the maximum *photon* hit density per train, *i.e.,* before conversion, the background would seem to be completely manageable for a pixel-based vertex detector.

At this point, the lesson we can draw from these studies is that having a beam-pipe radius less than 2 cm will require a field strength greater than 2 T. Most of the photons produced come from the interaction of the pairs with the beam pipe and from backscattering from the surfaces which are the closest in z to the IP, namely the luminosity monitor at z = 190 cm, the front face of the quadrupole doublet at 2 m, and the septum of the rf shield, currently at 189 cm. The IR design should pull back the the beam pipe to a larger radius as soon as it is past the maximum z required by the vertex detector, limited only by wakefield considerations to have a smooth transition from the FF quadrupole inner aperture to the beam pipe. If, when all residual questions as to the normalization of the simulation are understood, the effect of the photon hits in the central tracker are supportable, we may be able to decrease the distance between the IP and the quadrupole face, which would make the FF optical design much easier. At present the conical tungsten

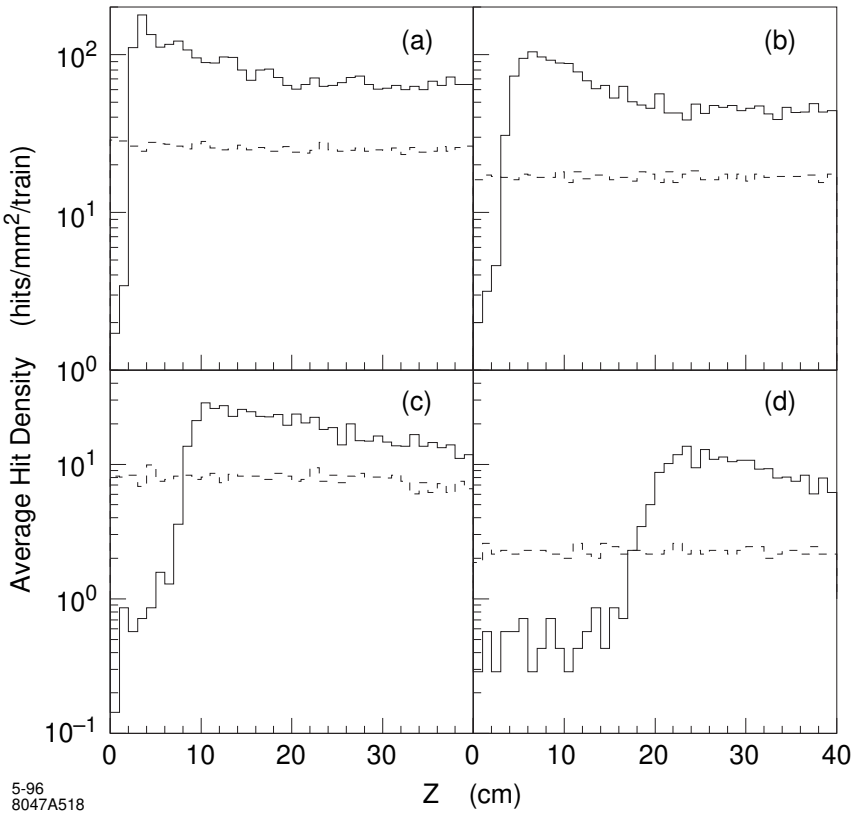

Figure 12-23. *The electron pair hit density per mm^2 per train of 90 bunches as a function of z. The solid line counts hits in scoring planes as the pairs leave the IP; the dashed line counts hits in the scoring planes resulting from the low p_t particles that have gone forward and hit the quad faces, septum, and luminosity monitor. The four parts correspond to: a) $r = 1$ cm and $B = 2T$, b) $r = 1$ cm and $B = 4T$, c) $r = 2$ cm and $B = 2T$, and d) $r = 2$ cm and $B = 4T$. The result is an EGS4 calculation using as input the ABEL beam-beam simulation at a center-of-mass energy of 1 TeV. In each case the scoring plane has an angular acceptance corresponding to* $\cos\theta = 0.90$.

mask M1 between 100 and 150 mr seems completely adequate to shield against pair induced backgrounds. The long tungsten skirt around the quadrupole pair, mask M2, appears necessary in the z area around the quadrupole face. It does not appear to be necessary that M2 neither be 3-m long, nor 10-cm thick.

Synchrotron Radiation Backgrounds

Section 12.3.3 discusses in detail the photon flux incident on the inner aperture of QFTA for the various lattice and final quadrupole options under discussion. Since, as described there, the synchrotron radiation from the Gaussian beam can be reduced to a negligible level by using an upbeam collimator, the detector backgrounds were calculated only for the synchrotron photons from the 1% flat-tail. The photon flux and energy spectrum of the tail described in Section 12.3.3 were used as an input for the EGS simulation.

Most of the photons incident on the inner surface of QFTA are absorbed in the quad, and particles penetrating the magnet can be stopped by Mask M1 and M2. However, the synchrotron photons hitting within about

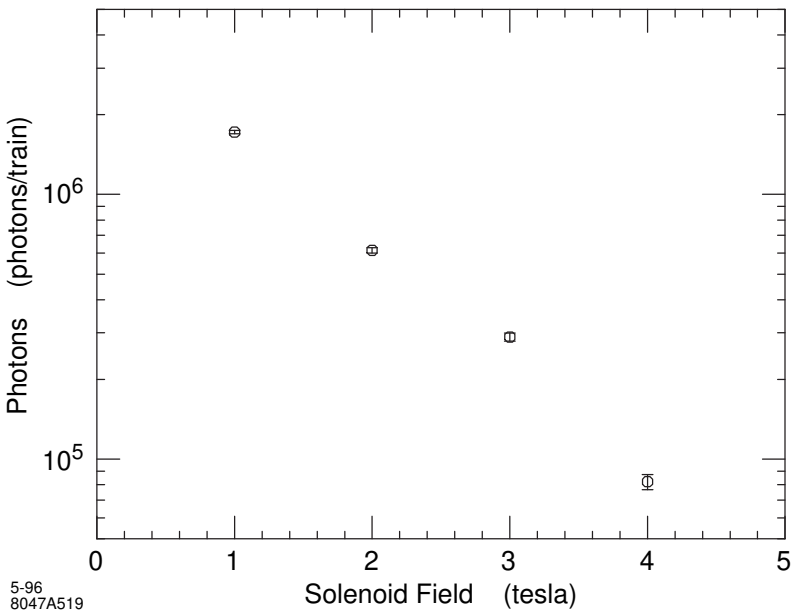

Figure 12-24. *The number of photons that strike a scoring plane at $r = 30$ cm arising from the interaction of e^+e^- pairs produced by the beam-beam interaction. The number of hits is shown as a function of the detector's solenoid field for center-of-mass energy of 1 TeV.*

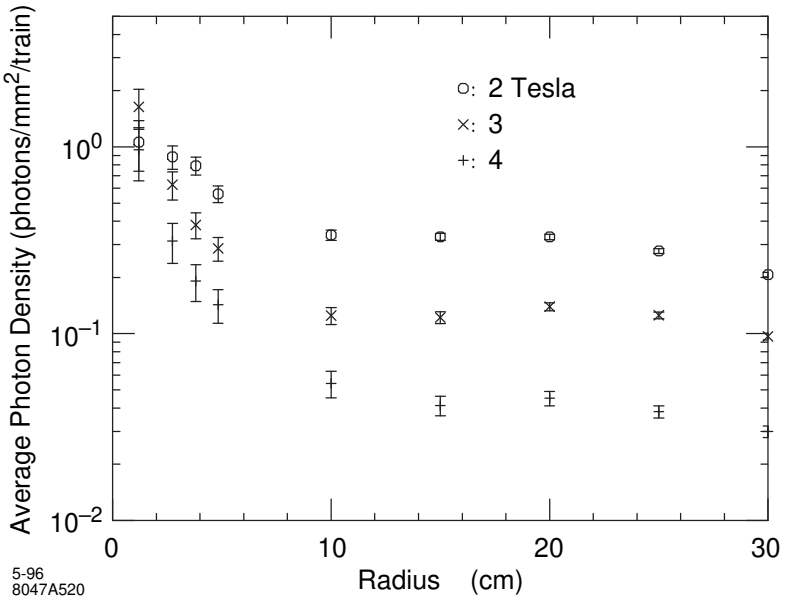

Figure 12-25. *The number of photons per train crossing that strike scoring planes at the indicated radii arising from the interaction of e^+e^- pairs produced by the beam-beam interaction. The number of hits is shown as a function of radius for three solenoid field strengths and 1 TeV center-of-mass energy.*

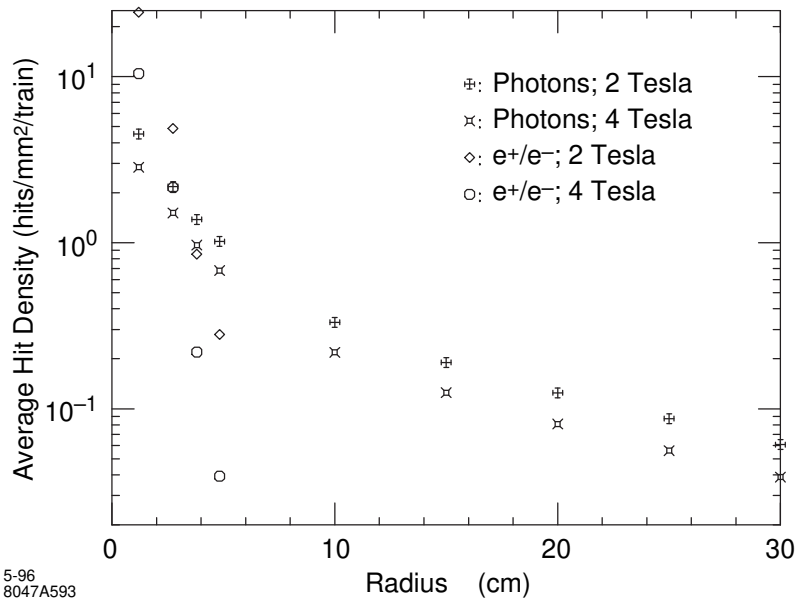

Figure 12-26. *The number of photons and e^+e^- hits per train crossing that strike scoring planes at the indicated radii arising from the interaction of photons in the inner bore of the QFTA quadrupole. These hits are produced by the quadrupole SR in the final focus lattice at 1-TeV-c.m. energy.*

10 cm of the quad exit produce secondary photons and electrons/positrons which come out of the quad and become a potential source of the detector backgrounds. The number of e^+e^- coming out of QFTA is 400K/train and the number of photons is 2×10^6/train. Those electrons/positrons that come out of the quad traverse the detector following the solenoid field and hit the vertex detector, while those secondary photons with angles between 10 and 30 mr with respect to the beam line interact with the vertex detector and rf shield within $z = \pm50$ cm or hit the downstream M1 face, contributing major backgrounds in the detector. Figure 12-26 shows the number of photon and electron/positron hits per mm^2 per train-crossing striking the vertex detector layers and massless scoring planes from $r = 1.2$ cm to $r = 30$ cm. The simulations were made for 2 and 4-T solenoid fields. At $r = 1.2$ cm, the e^+e^- hit density reaches as high as 10–20 hits/ mm^2 per train-crossing, and it may be intolerable even for a pixel-based vertex detector. While the photon density in the vertex detector is less than 5 photons/ mm^2 per train-crossing and is tolerable, the total number of photons striking the tracking chamber at $r = 30$ cm and z=±100 cm is 167K for 2 T and 110K for 4 T per train-crossing. The large photon flux may not be tolerable if we want to use a drift chamber.

The preliminary calculation described above has indicated that the SR backgrounds are potentially serious at $r = 1$ cm even for a pixel-base vertex detector and if a drift chamber is used. However, at 20–25-mm radius, such as that used by SLD at SLC, the situation is very much easier. While the backgrounds from the beam-beam interaction can be reduced by using a higher-strength solenoidal field, as shown in Figure 12-24, the SR backgrounds are not affected in the same way. Rather, the machine collimation and final-focus scheme must be designed so that the photon flux striking the inner surface of QFTA is substantially reduced. Furthermore, at 500 GeV-center-of-mass-energy, the likely startup point for an NLC, the number of SR photons goes down a factor of 2 and the average energy of the photons goes down a factor of 6, reducing the severity of this background source substantially.

Track Reconstruction Limits to the IR design

We will assume for the present that the innermost tracking detector will be a pixel-based device. The SLD has found that its vertex detector, VXD2, effectively composed of two layers of CCDs with 22 μm $\times$ 22 μm pixels, is very robust against the backgrounds seen at the SLC, which result in average occupancies at the level of 10^{-4}, or 0.4 hits per mm^2, summed over its readout of 19 beam crossings. SLD is currently installing a new vertex detector, VXD3, consisting of three layers of larger, less massive CCDs with the same pixel size. The extra layer will allow VXD3 to be a self-tracking device. VXD3 serves as an excellent model for an NLC detector inner tracking device.

To begin to estimate quantitatively the effects of backgrounds on track reconstruction, we have employed the detailed VXD3 Monte Carlo simulation and the standard SLD track reconstruction code to study the efficiency and purity for reconstructing the correct tracks resulting from hadronic Z^0 decays at resonance as a function of the density of randomly generated background hits. The mean number of tracks in the VXD3 acceptance is approximately 15. The standard SLD track reconstruction code begins with a track found in the SLD central drift chamber. For the purposes of this study, the Monte Carlo tracks were smeared appropriately and track banks formed to simulate a central tracking device. These tracks are then extrapolated to the VXD3 and linked to pixel clusters layer-by-layer using a Kalman Filter technique. Pixel clusters (hits) in the VXD3 resulting from background can affect the reconstruction procedure in two ways: background hits can merge with real hits acting to worsen the resolution, and background hits can cause track mislinks which can pull the track away from the real hits. The purity of the VXD3 linked hits, defined as the ratio of the number of real Monte Carlo hits to the total number of hits linked per track, measures the former effect. The efficiency of linked VXD3 hits, defined as the ratio of the number of hits linked to the number of hits expected to link per track, measures the latter effect. Figures 12-27 and 12-28 show how the efficiency and purity vary as a function of background hit density ranging from 0 hits/ mm^2 to 1 hit/ mm^2. Both the purity and efficiency drop only a few percent across this range display the robustness of this procedure against random backgrounds in the VXD3. This work is currently being extended to study the ability to tag B mesons resulting from top and Higgs production at 500-GeV-c.m. energies. This study will continue to use VXD3 as a model vertex detector, but will use a field strength of 2 T as well as using typical resolution and efficiency parameters for the NLC detector central tracking device. It is hoped to employ the B mass tagging algorithm which has become successful at the SLD.

12.4.2 Vibration Suppression for the Final Focus Quadrupoles

A schematic of the interaction region is presented in Figure 12-29, and indicates the four quadrupoles nearest the IP for the incoming beam. Also indicated are approximate locations of the detector tracking, calorimetry and muon identification systems, and the detector solenoidal coil. The quadrupole nearest the IP, QA, is a permanent magnet; Q1 is a superconducting magnet; and the two Q2 magnets are normal magnets. QA and Q1 are vertically focusing, while the Q2s are horizontally focusing. For a 5-nm vertical spot size at the IP, the tolerances for uncorrelated vertical vibrations of QA and Q1 are at the nm level. The vertical vibration tolerances for the Q2 magnets are about a factor of 3 less severe.

QA is chosen to be a permanent magnet to achieve a transversely compact magnet with the high-focusing gradient field needed. (Note that the separation of the incoming and outgoing beams is only 40 mm at z = 2 m from the IP.) Q1 is superconducting to allow tuning of the final focus at different beam energies. The drift distance from Q1 to the IP, l^*, is chosen to be 2 m due to geometric constraints and to allow space for vertex and luminosity detectors. QA must not be located in the fringe field region of the detector solenoid,

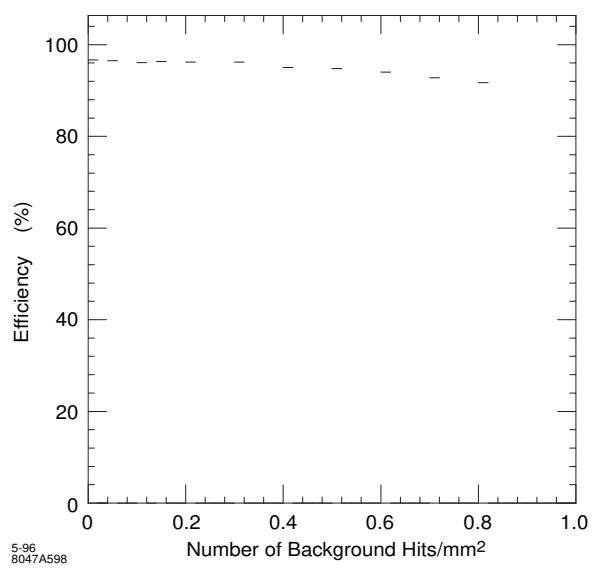

Figure 12-27. *Track efficiency vs. background level.*

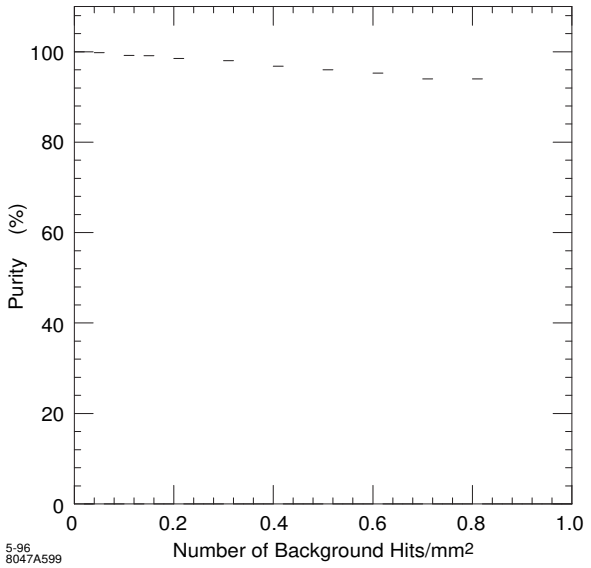

Figure 12-28. *Track purity vs. background level.*

since strong transverse fringe fields can demagnetize it. QA and Q1 are located well within the detector volume and will need to be supported from it.

The Q2 magnets are located outside the detector volume. Though their vibration tolerances are rather severe, we will assume that these magnets can be anchored mechanically to bedrock in the tunnels leading to the IP. As discussed in Appendix C and below, seismic motion in bedrock has a negligible impact on the NLC luminosity. We will not consider further the vibration stability issues for Q2, but will now focus our attention on the more difficult situation for QA and Q1. Figure 12-29 proposes that QA and Q1 be linked by optical transport arms of a laser interferometer to bedrock. This will be discussed below.

Appendix C gives a detailed description of the theory and measurement of ground motion. As is discussed there, the quadrupole alignment tolerances are very insensitive to disturbances with wavelengths which are long compared to the local lattice betatron wavelength. The dominant seismic effect is due to the microseismic peak, which has an amplitude of about 100–200 nm and a frequency of about 0.15 Hz. The wavelength of this disturbance, however, is many kilometers and so does not cause a relative misalignment of the final focus quadrupoles. Disturbances with frequencies below 1 Hz show highly correlated motion over separations of up to hundreds of meters, and the residual uncorrelated motion for the opposing final focus quadrupoles should be correctable by means of slow feedback. This feedback can monitor the deflection angles of the colliding beams to determine corrections to be made to the incoming beam trajectories. For frequencies above 1 Hz, seismic motion at quiet sites is less than 1 nm and therefore less than the tolerance for the final focus quadrupoles. Thus, if one could fix the FF quadrupoles to bedrock tens of meters below the earth's surface, seismic motion would have a negligible effect on colliding beam luminosity.

In practice, the final quadrupoles will be mounted inside a large particle detector. The structural characteristics of such a detector weighing thousands of tons and housing many layers of particle-detection apparatus in a strong 2–4-T magnetic field are similar to those of a large cube of gelatin at the nanometer scale. It will not be possible to construct independent supports for the final quadrupoles since the detector encloses nearly 4π of solid angle around the collision point. The final quadrupoles will have to be supported from the

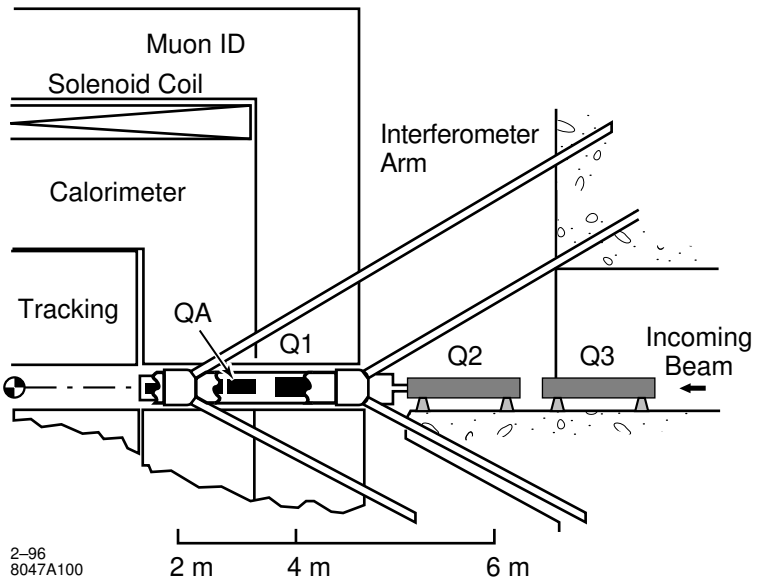

Figure 12-29. *IR final-focus quadrupoles.*

detector. Changing thermal gradients, cooling-system noise, cultural noise, and amplification of noise sources by the mechanical structure of the detector and quadrupole supports, will all contribute to mechanical noise.

Measurements made at SLAC (Section 12.4.5) and elsewhere indicate that even with good mechanical design, one may expect residual vibrations for the final quadrupoles at the level of 50-nm rms for frequencies above 1 Hz. This level of vibration will have to be measured and corrected to better than 1 nm.

Both optical and inertial measurement techniques are feasible for detecting sub-nm motion. The inertial devices are described in Appendix C. and these have been used extensively at SLAC and elsewhere to characterize ground motion. However, it may not be feasible to use these devices for the final quads that are buried inside the magnetic field of a large particle detector. An alternative method is to use a laser interferometer. A description of how to measure sub-nm displacements with an interferometer is given in Section 12.4.3, and a preliminary description for how to use such a device to stabilize the final quads is described in Section 12.4.4.

If motion of the final quadrupoles buried inside the detector can be measured with respect to bedrock, there are several approaches to stabilization. One indirect method would apply these signals to an external correction magnet to stabilize beam trajectory either by dithering its current or by piezoelectric positioning. A more direct approach would be active piezoelectric positioning of the final quadrupoles themselves. This approach has all the advantages of linearity and stability intrinsic to direct closed-loop feedback regulation around a null.

A number of activities are currently planned to address vibration issues for the IR. These include more measurements of vibrations of quadrupoles in the FFTB. The FFTB is also planning to commission an rf BPM capable of measuring beam position and beam jitter to better than 10 nm. If this is successful, they can try to correlate the beam jitter with the quadrupole jitter, and if a correlation is observed to try to correct for it. More vibration measurements are needed to try to quantify effects of cultural noise and vibration amplification by mechanical structures. Simulation work is needed to understand the vibration measurements being made and to develop engineering guidelines for a mechanical design of the IR and

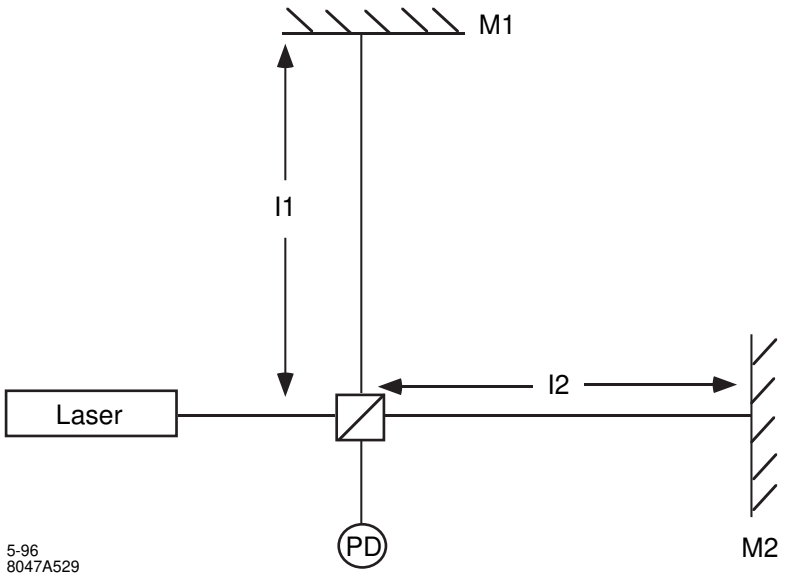

Figure 12-30. *A simple laser interferometer.*

Detector. In Sections 12.4.3 and 12.4.4, we describe an interferometer scheme to optically anchor the FF quadrupoles to bedrock. We plan to propose developing such a scheme with a mockup of an FF quadrupole to demonstrate that 50-nm vibration jiter can be measured and corrected for. This proposal will require developing independently a laser interferometer to measure the jitter and a piezo-mover system to correct it. The complete mockup would integrate a simulated FF quadrupole with its interferometer and piezo-mover systems.

12.4.3 Measurement of Sub-nm Displacements by means of a Laser Interferometer

The relative displacement of two objects at the subnanometer level can be measured by a laser interferometer. The LIGO experiment [Abramovici, 1992] proposes to measure the relative displacement of two masses, separated by 10 km, to a precision of 10^{-18} m. At the NLC, we only need to measure the relative displacement of the final quadrupole doublets, separated by 10 m, to a precision of 10^{-9} m. This may seem easy by comparison, but the geometry and accessibility of the final quadrupoles, buried inside the NLC detector, is much more complex. LIGO sensitivity will be at frequencies greater than 100 Hz, while the NLC is sensitive to frequencies below 50 Hz, where motion amplitudes are much greater. The measurement technique proposed by LIGO uses a laser interferometer somewhat more complex than the one indicated in Figure 12-30, but this figure serves to illustrate the measurement technique.

In Figure 12-30, we wish to detect relative changes in the lengths of the optical arms, l_1 and l_2, by monitoring intensity changes on the photodiode. The photodiode signal is given by

$$\begin{aligned} I &= N_\gamma(1+\cos\Phi) \\ \Phi &= \Phi^0 + \delta\Phi \end{aligned} \tag{12.10}$$

where N_γ is the number of incident photons, Φ^0 is the equilibrium phase difference between the two interferometer arms, and $\delta\Phi$ is due to changes in $(l_1 - l_2)$. The intensity change at the photodiode due to a change in $(l_1 - l_2)$, is given by

$$\begin{aligned} \delta I &= N_\gamma \sin\Phi^0 \delta\Phi \\ \delta\Phi &= 2\pi \cdot \frac{\delta(l_1 - l_2)}{\lambda} \end{aligned} \tag{12.11}$$

where λ is the wavelength of the laser light. One can choose to set $\sin\Phi^0 = 1$, in which case one gets

$$\frac{\delta I}{I} = \delta\Phi \quad . \tag{12.12}$$

For $\lambda = 633\,\text{nm}$, and $\delta(l_1 - l_2) = 1\,\text{nm}$, one will have $\delta\Phi = 0.02$ and this will cause a 2% intensity change on the photodiode.

There are many tolerances to be satisfied by the laser and optical system in this interferometer. These include tolerances on the laser's intensity stability, frequency stability and power. There are also tolerances on pressure and temperature fluctuations in the optical transport arms, which require that the transport arms be evacuated.

The laser intensity stability is required to be less than 2% for sub-nanometer displacement measurements. (Actually, the photodetector and its signal processor can be configured to detect and correct for laser intensity fluctuations. However, lasers with 1% intensity stability are commercially available.)

To determine the frequency stability required, we assume that the two optical path lengths can be equalized to better than 1 mm. Then

$$\begin{aligned} \frac{\Delta f}{f} &< \frac{10^{-2}}{2\pi} \times \frac{633 \times 10^{-9}}{2 \times 10^{-3}} \\ \frac{\Delta f}{f} &< 5 \times 10^{-7} \end{aligned} \tag{12.13}$$

The laser must have sufficient power that photon statistics will not cause significant noise in the measurement. For frequencies up to 100 Hz, we require

$$\begin{aligned} P &> \frac{(10^{-2})^2\gamma}{10^{-2}\text{sec}} \times \frac{2\text{eV}}{\gamma} \times (1.6 \times 10^{-19}\frac{\text{J}}{\text{eV}}) \\ P &> 3.2 \times 10^{-13}\ \text{W} \end{aligned} \tag{12.14}$$

Pressure fluctuations in the laser transport arms will cause a change in the index of refraction, n, and hence a change in the optical path length. In air, the dependence of the index of refraction on pressure and temperature is given by $(n-1) = 1.2 \times 10^{-4}[P(\text{Torr})/T(^\circ\text{K})]$. An optical path length of 15 m and a temperature of 300°K, will require $\Delta P < 10^{-4}$ Torr.

Temperature fluctuations will cause a change in the optical path length due to the strain coefficients for the mirrors and beam splitter. If we assume a strain of 10^{-6} per °C, then a 1-cm-thick optic can change the path length by 10nm/°C. Thus, the temperature will need to be stabilized to 0.1°C.

A laser which satisfies these requirements is a commercially available frequency-stabilized HeNe, with the following characteristics:

$$f = 473.61254\ \text{THz} \tag{12.15}$$

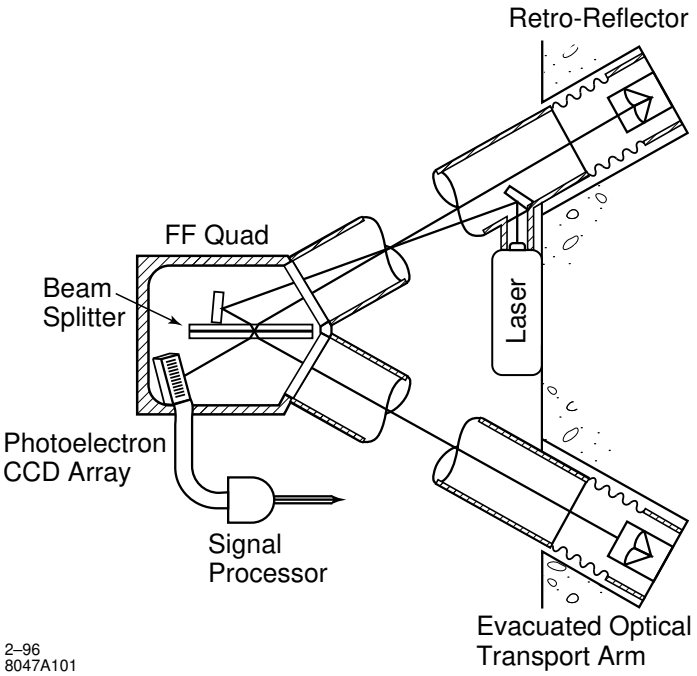

Figure 12-31. *Interferometer for Optical Anchoring of an FF quadrupole.*

$$\frac{\Delta f}{f} < 10^{-8} \tag{12.16}$$

$$\frac{\Delta I}{I} < 5 \times 10^{-4} \tag{12.17}$$

$$P = 1\,\mathrm{mW} \tag{12.18}$$

$$\mathrm{Cost} < \$4000 \tag{12.19}$$

12.4.4 An Optical Anchor for the Final Quadrupoles

To gain the necessary stability for collision of nanometer beams, the final quadrupoles must be rigidly connected to bedrock outside the detector. This has been done in the past by optical interferometry. [Wyatt, 2982] The final quadrupoles could be anchored to points buried deep into the walls of the detector hall by building arms of an interferometer out from the final quadrupoles to corner cube reflectors mounted to stable rock. Optical paths are angled at 60° as shown below in Figure 12-31. (Note that the choice of a 60° angle is not critical, and that smaller angles can be chosen to work equally well.)

For a 60° geometry, the differential change in the optical path between the two arms d equals the transverse motion of the beam splitter S. Each quadrupole would require individual interferometers to measure y transverse motion (we assume that measurement and correction of x vibrations is not necessary). Optical transport arms from the quadrupole to bedrock retroreflectors would be 15–20-m long and would require vacuum pipes 60–80-mm in diameter out through the detector. For each QA or Q1 quadrupole, we assume that the quadrupole acts as a rigid body (not a trivial assumption for nanometer vibrations of a 1.5-m-long

quadrupole; we will need to investigate over what lengths this assumption is valid), and that independent interferometer systems will be needed to stabilize each end of a quadrupole.

As described in Section 12.4.3, a commercial frequency-stabilized HeNe laser can be used for this system. The photodetector and its signal processing system are required to detect phase changes corresponding to less than 1/500th of a fringe (*i.e.,* less than 1 nm). We are currently investigating commercial systems to do this, but it is possible this will need to be custom-built. There are at least two companies who appear to make appropriate piezo movers with sub-nanometer resolution and accuracy, and we are investigating the specifications for these.

12.4.5 SLD Final Focus Quadrupole Vibration Measurements

Preliminary results are available from vibration measurements of the SLD final focus quadrupoles. The SLD final focus quadrupoles are a superconducting triplet supported from SLD's endcap door. The measurements were made with the STS-2 seismometers described in Appendix C.

In the final-focus tunnel leading to the collider hall and SLD, the seismometers measured about 10 nm of rms vertical motion above f = 1 Hz. On the triplets themselves, the measurements were in the range of 30–50 nm of vertical rms motion above $f = 1$ Hz. These measurements were made with the solenoid cooling water on and the cryogenic He flow on. There was no observed effect from the He flow, though there appeared to be an effect due to the cooling water. The solenoid was not powered during these tests.

It appears that triplet vibrations do not cause loss of luminosity at the SLC where the beam sizes are greater than 500 nm. And it appears that one might expect vibrations for the final focus magnets inside an NLD to be on the order of 50 nm or less for $f > 1$ Hz. (One might expect less at a quieter geographic site, and when a support design is engineered giving consideration to vibrations at the 10-nm level.) If such is the case, this vibration would need to be measured and corrected for to about 1-nm accuracy. It also appears that superconducting magnets are acceptable in the final focus, so that one is not limited to permanent magnets.

12.4.6 Measurement of Polarization and Beam Energy

One key advantage of doing physics at the NLC is that the electron beam will be highly polarized. The experimental challenge is to measure this polarization accurately enough for the physics channel under study. At the SLC, this is accomplished to an accuracy of $\simeq 0.5\%$ by colliding the electron beam with a longitudinally polarized photon beam of known polarization and using the spin asymmetry in the cross section of the resulting $e\gamma$ Compton-scattering interaction to determine the beam polarization.

Two major mechanisms induce depolarization during the beam-beam interaction. They are discussed in Ref. [Yokoya, 1988]. These are the classical spin precession under the collective field of the oncoming beam, and the spin-flip effect from beamstrahlung (Sokolov-Ternov effect). The latter is typically the most serious problem. For the range of parameters of the collider designs under discussion, one can place the limit $\Delta P < 0.04 n_\gamma$. We need to determine the precision to which the polarization needs to be measured (this will later be moved to the Physics section being developed). The details of the polarization measurement are described in the Final Focus Chapter 11 Section 11.8 on the Extraction Line.

The SLC measures the beam momenta to 20 MeV, or about 0.05%, using a spectrometer-like system which measures the separation and width of two synchrotron radiation stripes produced before and after the beam

is bent by the field of a very well measured magnet. Again we need to specify the precision to which this needs to be measured. The details of the measurement are described in the Final Focus Chapter 11 Section 11.8 on the Extraction Line.

12.5 Conclusions

More work is needed at all levels. For example, the same tools used for the other background sources can be used to place limits on the allowable number of particles in the beam tails which may strike the quadrupole aperture. We have not discussed the possibility of using fast detector timing as a means of resolving background processes, nor the general question of how backgrounds will affect trigger rates. Backgrounds have not been discussed in the context of radiation damage to detectors.

References

[Abramovici, 1992] A. Abramovici *et al., Science* **256**, 325 (1992).

[Barklow, 1992] T. Barlow, P. Chen, and W. Kozanecki, "Beamstrahlung Spectra in Next Generation Linear Colliders", SLAC–PUB–5718 Rev., (April 1992).

[Chen, 1990] P. Chen and K. Yokoya, "Beam-Beam Phenomena in Linear Colliders", US/CERN School on Particle Accelerators (1990).

[Chen, 1992] Pisin Chen, Differential Luminosity Under Multiphoton Beamstrahlung, *Phys. Rev. D* **46**, 1186 (1992).

[Feldman] G. Feldman, MUCARLO, Version 1.0 (1988).

[Frary] M.N. Frary and D.J. Miller, in Ref. [Munich, 1991], p. 379.

[Helm, TLCFF28] R. Helm, Transport Deck TLCFF28.

[SLAC 1996] R. Jacobsen, *Proc. 1996 SLAC LC Physics Workshop*, (1996).

[TRC 1995] International Linear Collider Technical Review Committee Report 1995, G.A. Loew, Chairman, SLAC–R–95–471, (December 1995).

[Keller, 1991] L.P. Keller, "Calculation of Muon Background in a 0.5-TeV Linear Collider", SLAC–PUB–5533 (April 1991).

[Keller] L.P. Keller, Muon Background in a 1.0-TeV Collider, SLAC–PUB–6385 (October 1993).

[Kuraev, 1985] E.A. Kuraev and V.S. Fadin, *Sov. J. Nucl. Phys.* **41**, 466 (1985).

[Mokhov] N. Mokhov, MARS13 muon production and transport code.

[Peskin, 1991] M.E. Peskin and M. Strassler, *Phys. Rev. D* **43**, 1500 (1991).

[Wyatt, 2982] F. Wyatt, K. Beckstrom, and J. Berger, *Bull. Seismological Soc. of Am.* **72**, 1707 (1982).

[Yokoya, 1988] K. Yokoya and P. Chen, "Depolarization due to Beam-Beam Interaction in Electron-Positron Linear Colliders", SLAC–PUB–4692 (1988).

[Munich, 1991] P.M. Zerwas, ed., e^+e^-*-Collisions at 500 GeV: The Physics Potential, Parts A and B* (Workshops at Munich, Annecy, Hamburg, 1991), DESY 92-123A&B (1992).

Contributors

- G. Bowden
- M. Breidenbach
- R. Frey
- S. Hertzbach
- L. Keller
- T.W. Markiewicz
- T. Maruyama
- R. Messner
- T. Usher
- M. Woods